The Planetary Science Journal, 5:204 (15pp), 2024 September https://doi.org/10.3847/PSJ/ad7111

Ocean Circulation on Tide-locked Lava Worlds. I. An Idealized 2D Numerical Model

Yanhong Lai[1,2], Jun Yang[1,2], and Wanying Kang[3]

[1] Laboratory for Climate and Ocean-Atmosphere Studies, Department of Atmospheric and Oceanic Sciences, School of Physics, Peking University, Beijing 100871, People's Republic of China; junyang@pku.edu.cn

[2] Institute of Ocean Research, Peking University, Beijing 100871, People's Republic of China

[3] Department of Earth, Atmosphere and Planetary Science, MIT, Cambridge, MA 02139, USA

Received 2023 December 27; revised 2024 June 12; accepted 2024 July 1; published 2024 September 24

Abstract

A magma ocean is expected to exist on the dayside of tide-locked planets if surface temperature exceeds the melting temperature of typical crust. As highly prioritized targets for the James Webb Space Telescope, more information about the surface and atmosphere of lava planets will soon be available. In most previous studies of lava planets, the system is typically assumed to be vigorously convecting and isentropic. This implies a magma ocean depth reaching $\mathcal{O}(10^4\text{–}10^5)$ m, determined by the adiabats and melting curves. In this study, we aim to simulate ocean circulation and ocean depth on tidally locked lava worlds using an idealized 2D (x–z) model developed by the authors. Our simulation results show that under zero or a small internal source, the maximum zonal current speed ranges from 0.1 to 1.0 m s^{-1} and the magma ocean depth remains $\mathcal{O}(100)$ m, being more than 100 times shallower than that predicted in a fully convecting system. We demonstrate that the ocean heat transport divergence is consistently smaller than the stellar insolation by 1–2 orders of magnitude. Consequently, the impact of ocean circulation on the thermal phase curve of tidally locked lava worlds is minimal in observations.

Unified Astronomy Thesaurus concepts: Exoplanet dynamics (490); Exoplanets (498); Habitable planets (695)

1. Introduction

A hemispherical magma ocean can form and persist on tidally locked terrestrial exoplanets if the planets are very close to their host stars (A. Léger et al. 2009, 2011; E. S. Kite et al. 2016; K.-H. Chao et al. 2021). These planets, often referred to as "lava worlds," are more detectable owing to their high substellar temperature ($T_{\rm sub}$) and relatively large transit depth. A substantial number of lava planets have been identified,[4] such as Kepler-10b ($T_{\rm sub} = 3000$ K; N. M. Batalha et al. 2011; X. Dumusque et al. 2014), CoRoT-7b ($T_{\rm sub} = 2500$ K; A. Léger et al. 2009), 55 Cnc e ($T_{\rm sub} = 2773$ K; B.-O. Demory et al. 2011; V. Bourrier et al. 2018), TOI-561b ($T_{\rm sub} = 3218$ K; C. L. Brinkman et al. 2023), and K2-141b ($T_{\rm sub} = 3000$ K; L. Malavolta et al. 2018; T. G. Nguyen et al. 2020). Lava worlds are currently considered high-priority targets for the James Webb Space Telescope (C. A. Beichman & T. P. Greene 2018). Consequently, more observational data regarding the atmosphere and surface of lava planets will soon be available.

Due to the extremely high surface temperature and the relatively old age of lava worlds (e.g., ∼2 Gyr for CoRoT-7b and ∼10 Gyr for Kepler-10b; A. Léger et al. 2009; N. M. Batalha et al. 2011), it is possible that volatile elements (such as C, N, H) have escaped from the planets (D. Valencia et al. 2010), so that the atmospheric mass will be low. The tenuous atmosphere comes from the vaporization of underlying silicate melts (A. Léger et al. 2009; L. Schaefer & B. Fegley 2009; E. S. Kite et al. 2016). Under temperatures higher than the melting point, the magma surface initially outgasses the most volatile components to the atmosphere, until atmospheric partial pressure reaches an equilibrium with the surface. Atmospheric pressure is determined by surface temperature, peaking at the substellar point and ranging from 10^0 to 10^4 Pa, due to the strongest evaporation (A. Leger et al. 2011; T. G. Nguyen et al. 2020). It gradually approaches zero at the magma ocean boundary, where no evaporation occurs. Thus, there is a strong atmospheric pressure gradient, leading to strong winds flowing outward from the substellar point (∼2000 m s^{-1}; T. Castan & K. Menou 2011; T. G. Nguyen et al. 2020; W. Kang et al. 2021).

Given the tenuous atmosphere on lava planets, the effects of atmosphere on surface temperature are generally limited and negligible (A. P. Ingersoll et al. 1985; A. Leger et al. 2011; E. S. Kite et al. 2016; T. G. Nguyen et al. 2020). For molten silicates with a latent heat of vaporization $l_v \sim 10^5\text{–}10^6$ J kg^{-1} and a maximum evaporation rate $E \sim 0.1$ kg m^{-2} s^{-1} (T. G. Nguyen et al. 2020), a latent heat flux of 10^4–10^5 W m^{-2} can be calculated. This is about one or two orders of magnitude smaller than the stellar insolation (∼10^6 W m^{-2}; T. Castan & K. Menou 2011). Thus, the surface temperature of lava planets is typically assumed to be determined by local radiative balance (A. Léger et al. 2009).

Much remains unclear regarding the ocean on lava planets. Two primary theories aim to determine the magma ocean depth on tidally locked lava planets: adiabat determined and ocean circulation determined. In scenarios with strong internal heating, the interior heat source may dominate over stellar radiation, leading to robust vertical convection (C.-É. Boukaré et al. 2022). Vigorous convection establishes an isentropic and adiabatic vertical temperature profile, for which temperature increases with pressure following the adiabatic lapse rate (red line in Figure 1(a); V. Solomatov 2007; Y. Zhang et al. 2022). Magma ocean depth is determined by the intersection of this adiabatic temperature profile and the melting curve (black line in Figure 1(a); C. Herzberg & J. Zhang 1996; G. Fiquet et al. 2010; A. Leger et al. 2011). Consequently, the magma ocean

---

[4] https://exoplanetarchive.ipac.caltech.edu/docs/counts_detail.html

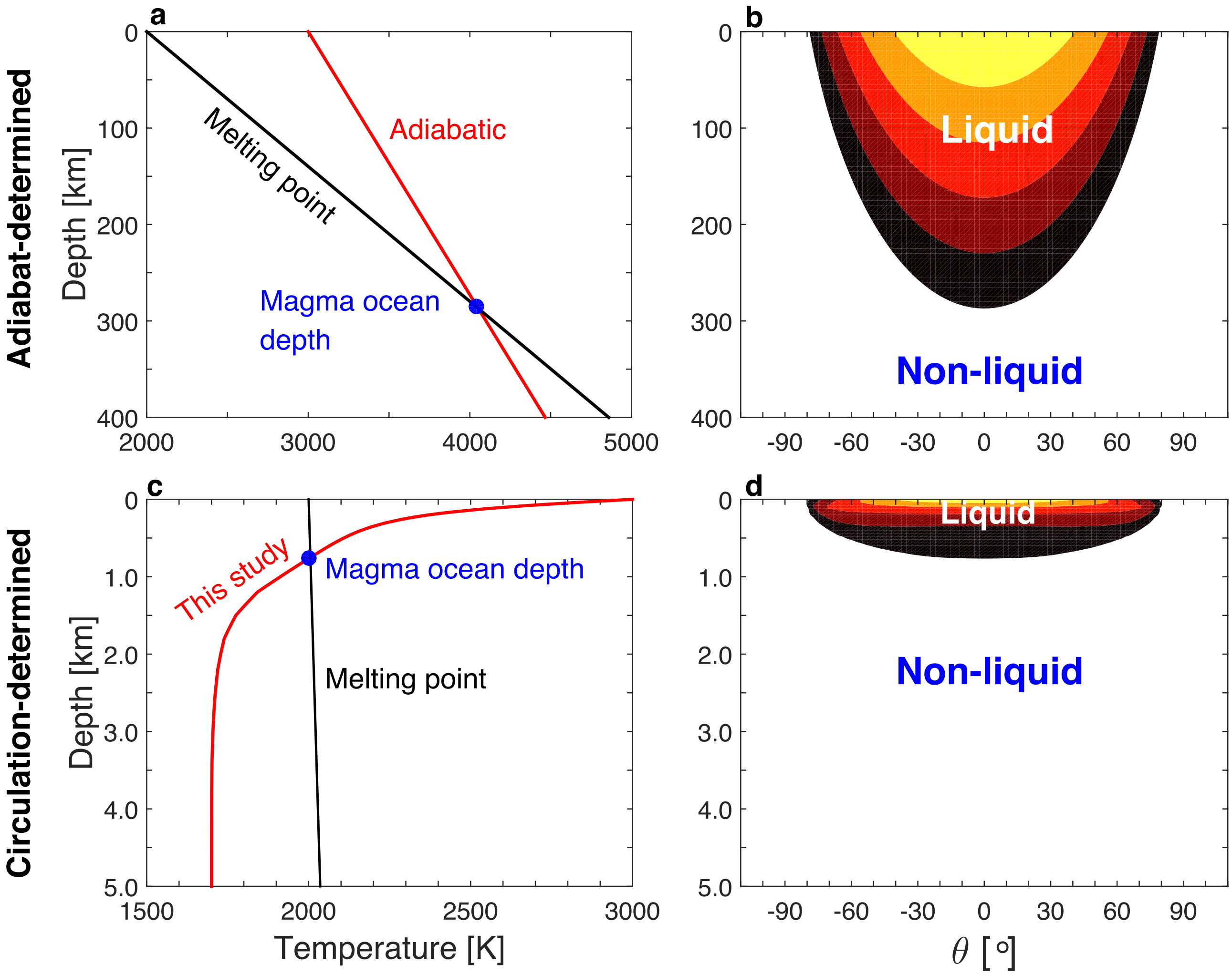

Figure 1. Vertical temperature profile and magma ocean depth when they are adiabat determined (top panels) and ocean circulation determined (bottom panels). (a, c) Vertical temperature profile with a substellar temperature of 3000 K (red line) and the liquidus curve (black line). (b, d) The magma ocean depth as a function of the angle away from the substellar point under a surface temperature shown in Figure 2(b). Note that the liquidus in panel (c) increases with depth as in panel (a), but it is not evident within the shallow depth. The vertical range is different between the top and bottom panels.

depth can reach tens to hundreds of kilometers (Figures 1(a) and (b); A. Leger et al. 2011; C.-É. Boukaré et al. 2022, 2023; T. G. Meier et al. 2023).

The interior temperature profile can become subadiabatic (i.e., the vertical temperature gradient is smaller than the adiabatic lapse rate), when the internal heat source is weak or absent. Under such conditions, the magma ocean may not exhibit vigorous convection. T. G. Meier et al. (2023) utilized 2D mantle convection models to investigate the potential magma ocean depth of 55 Cnc e under varying internal heating rates. Their findings indicate that the magma ocean depth determined by a subadiabatic temperature profile is significantly shallower compared to that governed by adiabatic and superadiabatic profiles. Nevertheless, the magma ocean depth still reaches approximately 500 km on the dayside, even without internal heating. The effect of ocean circulation on magma ocean depth was not included in their study.

Magma ocean depth will be governed by ocean circulation when the internal heat source is weak or absent. This scenario is possible for tidally locked lava planets, especially those that have cooled over gigayears (such as CoRoT-7b, Kepler-10b, 55 Cnc e; A. Leger et al. 2011; N. M. Batalha et al. 2011; K. Von Braun et al. 2011; L. Malavolta et al. 2018; C. L. Brinkman et al. 2023). The overturning circulation is possible on lava planets, given that the viscosity of molten silicates is comparable to that of seawater in Earth's oceans (D. B. Dingwell et al. 2004; W. M. Haynes 2014; Y. Sun et al. 2020; Y. Zhang et al. 2022). With a large surface temperature gradient and strong atmospheric winds (A. Leger et al. 2011; T. Castan & K. Menou 2011), thermal-driven and wind-driven overturning circulation similar to Earth's oceans could exist within the magma ocean. As suggested by E. S. Kite et al. (2016), magma ocean depth in the presence of a thermal-driven overturning circulation might be over 100 times shallower than that determined by the adiabats. However, their magma ocean depth was obtained using scaling analysis, and numerical simulations for how ocean circulation reduces magma ocean depth are lacking. Furthermore, the effect of wind forcing was not taken into account. Numerical simulations of magma oceans on tidally locked lava planets are strongly needed.

To simulate ocean circulation on lava planets, general circulation models (GCMs), such as MITgcm (J. Marshall et al. 1997a, 1997b), face three main challenges. First, the ocean depth, marking the boundary between liquid and nonliquid regions, continuously evolves with temperature until equilibrium is reached. Second, due to the extensive temperature range on lava planets, silicates exist in three different states: solid, partially molten, and liquid. Thus, it is necessary to account for the variation of silicate viscosity and diffusivity with temperature (D. B. Dingwell et al. 2004; D. B. Ghosh & B. B. Karki 2011; H. Ni et al. 2015). In current GCMs, only constant values or prescribed spatial patterns for viscosity and diffusivity are available. Third, silicate viscosity also changes drastically with melt fraction, varying from 10^{18} to 10^{-4} m^2 s^{-1} from the solidus (melt fraction is zero) to the liquidus (melt fraction is 100%; see Section 2.2). The large value and variation of viscosity can easily lead to numerical instability.

Here we simulate the ocean overturning circulation on tidally locked lava worlds using an idealized two-dimensional (2D, x–z) model that we developed. Note that only a small internal heat source (0.5 W m^{-2}, corresponding to a temperature of 50 K on the nightside; A. Leger et al. 2011) is included in this study, given that most tidally locked lava worlds have cooled over billions of years. We present detailed model descriptions and experimental designs in Section 2. In Section 3.1, the ocean circulation and magma ocean depth with thermal forcing only are shown. Section 3.2 presents simulation results with both thermal and wind forcings. The comparison between our study and previous studies is discussed in Section 3.3. Implications of our results for future observations are discussed in Section 3.4. In Section 4, we discuss the potential influence of varying factors on the simulation results. In Section 5, we summarize the results.

It is important to note that the magma ocean investigated in this study differs from the global magma ocean formed during the formation of rocky planets, such as early Mars and early Earth (L. T. Elkins-Tanton 2012; J. Monteux et al. 2016). The magma ocean on tidally locked lava planets is long-lived owing to persistent stellar insolation. In contrast, the cooling and crystallization of the magma ocean formed in the early planetary evolution is a rapid process, with a solidification time ranging from thousands to millions of years (K. Hamano et al. 2015; J. Monteux et al. 2016; A. Nikolaou et al. 2019).

2. Model Descriptions and Experimental Designs

We simulate the magma ocean using a self-developed 2D (x–z) model programmed in Matlab 2019a. For simplicity, the y-direction is not resolved, and the meridional velocity is assumed to be zero everywhere. The effect of planetary rotation is also excluded in the 2D model. Referring to the 3D equations employed in MITgcm (a global ocean model for oceans on Earth; J. Marshall et al. 1997a, 1997b), the 2D governing equations for the magma ocean on lava worlds in the Cartesian coordinate can be written as follows:

$$\frac{\partial u}{\partial t} + u\frac{\partial u}{\partial x} + w\frac{\partial u}{\partial z} = -\frac{1}{\rho_c}\frac{\partial p}{\partial x} + \frac{\partial}{\partial x}\left(A_h\frac{\partial u}{\partial x}\right) + \frac{\partial}{\partial z}\left(A_z\frac{\partial u}{\partial z}\right) + F_u, \quad (1)$$

$$\frac{\partial \theta}{\partial t} + u\frac{\partial \theta}{\partial x} + w\frac{\partial \theta}{\partial z} = \frac{\partial}{\partial x}\left(k_h\frac{\partial \theta}{\partial x}\right) + \frac{\partial}{\partial z}\left(k_z\frac{\partial \theta}{\partial z}\right) + F_\theta, \quad (2)$$

$$\frac{\partial u}{\partial x} + \frac{\partial w}{\partial z} = 0, \quad (3)$$

$$\frac{\partial \eta}{\partial t} + \frac{\partial H\hat{u}}{\partial x} = 0, \quad (4)$$

$$T = T(\theta, p), \quad (5)$$

$$\rho = \rho(T, p);\ \rho_s = \rho(T_s, 0), \quad (6)$$

$$p = \rho_s g\eta + \int_z^0 \rho g dz, \quad (7)$$

$$A_h = A_h(T);\ A_z = A_z(T), \quad (8)$$

where x is the horizontal distance from the substellar point; z is the vertical distance from the surface and is negative; u and w are zonal and vertical current speeds, respectively; θ and T are potential temperature and temperature, respectively; ρ is ocean density; ρ_c is the reference density, and a value of 2600 kg m^{-3} is used; T_s and ρ_s are temperature and density at the surface, respectively; η is sea surface height (SSH), which is determined by the vertical integral of the horizontal divergence of the zonal velocity ($\frac{\partial H\hat{u}}{\partial x}$, where $H\hat{u} = \int_{-H}^{\eta} u dz$ and H is the depth of the vertical domain); g is gravity; p is pressure, which is composed of a barotropic part due to variations in surface height (η) and a hydrostatic part due to the vertical integral of density (ρ); A_h and A_z are horizontal and vertical viscosity coefficients, respectively; k_h and k_z are horizontal and vertical diffusivities, respectively; and F_u and F_θ are zonal wind forcing and surface temperature forcing, respectively.

In a multicomponent system (L. Schaefer & B. Fegley 2009; M. Zilinskas et al. 2022), silicates exhibit different states based on temperature (D. J. Stevenson 2010). They are solid when the temperature is below the solidus, partially molten between the solidus and liquidus, and fully molten when the temperature is above the liquidus. Partially molten silicates exhibit solid-like behavior when the crystal fraction exceeds a critical threshold, while behaving more fluid-like when the crystal fraction falls below this threshold. This critical value is highly dependent on the rheology (e.g., the crystal composition, size, and shape, etc.; A. Lejeune & P. Richet 1995; M. D. Rintoul & S. Torquato 1996; A. Costa 2005; Y. Zhang et al. 2022). Both the solidus and liquidus increase with increasing pressure (J. Monteux et al. 2016; Y. Zhang et al. 2022). Due to the shallow depths (see below), their variations are limited. Therefore, both the solidus ($T_{\rm sol}$) and liquidus ($T_{\rm liq}$) are considered as constants in this study. By default, $T_{\rm sol} = 1700$ K and $T_{\rm liq} = 2000$ K (J. Monteux et al. 2016). It is worth mentioning that the melting temperature of silicates rises if the solid interior of the planet is depleted in volatiles, which might threaten the persistence of the magma ocean (S. E. Gelman et al. 2011). This scenario could occur on tidally locked lava worlds, given that their magma oceans have vaporized over billions of years.

It is important to note that Equation (2) predicts potential temperature rather than the absolute temperature. To determine silicate density and viscosity (Equations (6) and (8)), a conversion from potential temperature to temperature following the adiabatic lapse rate is required (Equation (5); N. Fofonoff 1962; T. J. McDougall & R. Feistel 2003). The difference between potential temperature and temperature is limited, compared to the temperature itself.

2.1. Equation of State

The equation of state (EOS) characterizes the dependence of silicate density on temperature and pressure, typically determined using the third-order Birch–Murnaghan EOS (T. Katsura et al. 2010; T. Sakamaki et al. 2010). To simplify,

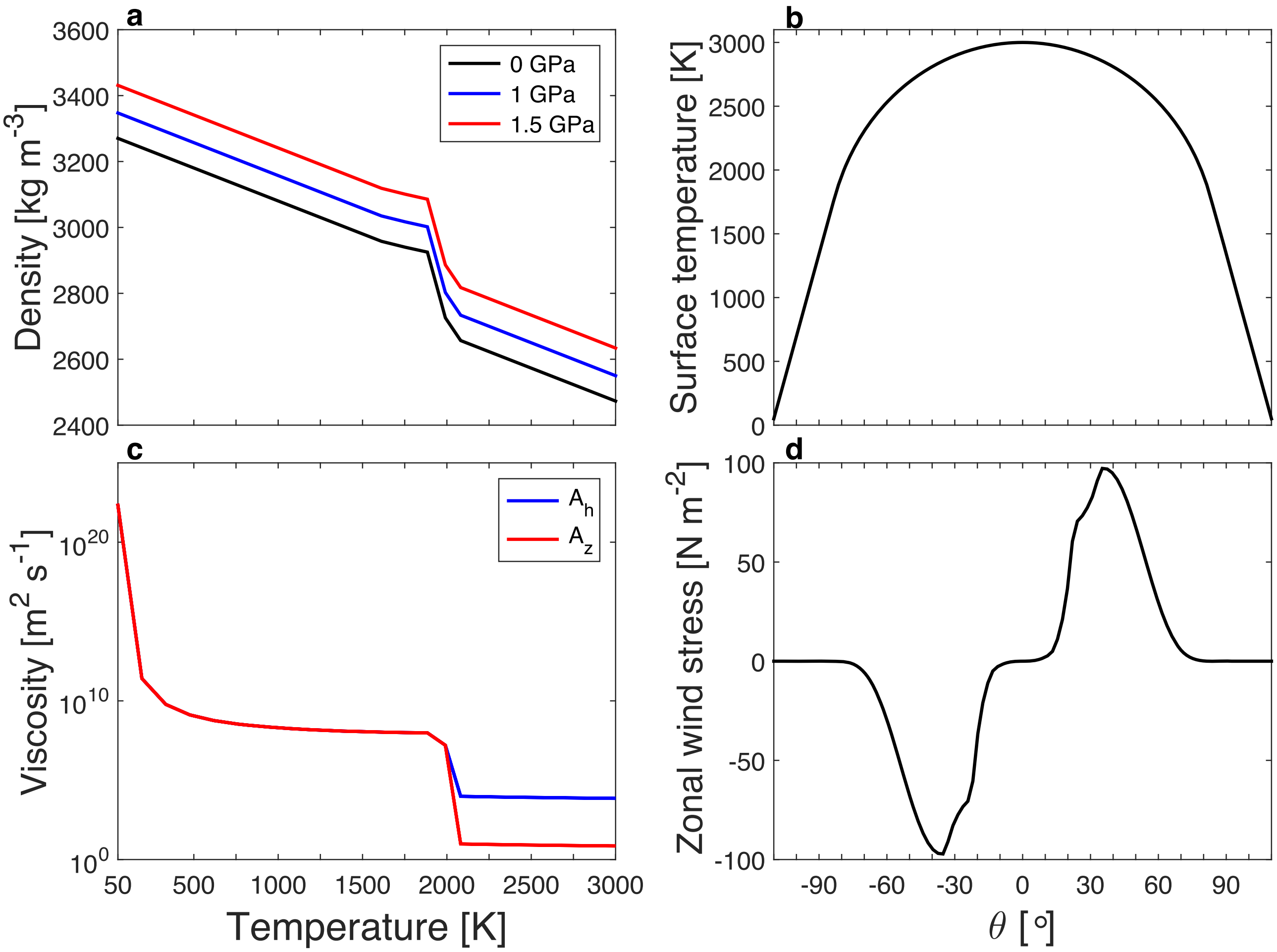

Figure 2. (a) EOS used in the model; (c) horizontal (A_h) and vertical (A_z) viscosity coefficients as a function of temperature. (b) External forcings imposed at the surface. Surface temperature with a substellar temperature of 3000 K and a temperature of 50 K at ±110°; (d) zonal wind stress with a maximum value of ~100 N m^{-2} near 40°, where a positive (negative) value corresponds to eastward (westward) wind stress.

linear and quadratic approximations are employed to represent the relationship between density and temperature and that between density and pressure, respectively (Equation (6) and Figure 2(a)). These approximations are based on fitting the third-order Birch–Murnaghan EOS. To calculate density, the densities at the liquidus (ρ_{l0}) and at the solidus (ρ_{s0}) at zero pressure are defined, respectively, as

$$\rho_{l0} = \rho_0 + \alpha_1(T_{\text{liq}} - T_0),\ \rho_{s0} = \rho_{l0}(1 + \Delta\rho), \tag{9}$$

where $\rho_0 = 2.673\ \text{g cm}^{-3}$ is the reference density at a reference temperature ($T_0 = 2000$ K) and at zero pressure, $\alpha_1 = -2 \times 10^{-4}\ \text{g cm}^{-3}\ \text{K}^{-1}$ is the slope of density with temperature, and $\Delta\rho = 10\%$ is the density difference between the solidus and liquidus (N. Tosi et al. 2013; D. B. Ghosh & B. B. Karki 2016). Then, the interior density can be given as

where ρ_s, ρ_t, and ρ_l are the densities in solid, transitional, and liquid states, respectively; β_1 and β_2 are constant parameters determining the variation of density with pressure, with values of $0.00667\ \text{g cm}^{-3}\ \text{GPa}^{-2}$ and $0.1022\ \text{g cm}^{-3}\ \text{GPa}^{-1}$, respectively; and c_1 and c_2 are parameters set to ensure the continuity of density with temperature in different temperature ranges, satisfying $\tanh(c_1) = 1$ and $\tanh\left(\dfrac{\rho_l(T = T_{\text{liq}})}{\rho_s(T = T_{\text{sol}})}\right) = c_2$, where c_2 is nonconstant and varies with pressure. Note that ρ is in g cm^{-3} and pressure is in GPa (10^9 Pa) in Equations (9) and (10). Equation (10) and Figure 2(a) show that density decreases linearly with increasing temperature when the temperature is below the solidus or above the liquidus. In the range between the solidus and liquidus, density decreases with temperature following a hyperbolic tangent (tanh) function. Furthermore, density always increases quadratically with increasing pressure.

$$\rho = \begin{cases} \rho_s = \rho_{s0} + \alpha_1(T - T_{\text{sol}}) + \beta_1 p^2 + \beta_2 p, & T < T_{\text{sol}} \\ \rho_t = (\rho_{s0} + \beta_1 p^2 + \beta_2 p) \cdot \tanh\left(c_1 - (c_1 - c_2)\dfrac{T - T_{\text{sol}}}{T_{\text{liq}} - T_{\text{sol}}}\right), & T_{\text{sol}} \leqslant T < T_{\text{liq}}, \\ \rho_l = \rho_{l0} + \alpha_1(T - T_{\text{liq}}) + \beta_1 p^2 + \beta_2 p, & T \geqslant T_{\text{liq}} \end{cases} \tag{10}$$

2.2. Viscosity and Diffusivity

Silicate viscosity is dependent on pressure and temperature approximately following an Arrhenius relationship (D. B. Dingwell et al. 2004; C. Liebske et al. 2005; D. B. Ghosh & B. B. Karki 2011). The effect of pressure on silicate viscosity is relatively small and can be ignored (C. Liebske et al. 2005). Silicate viscosity also changes drastically with melt fraction, ranging from 10^{18} to $10^{-4}\,\mathrm{m^2\,s^{-1}}$ from the solidus to liquidus (Y. Sun et al. 2020; Y. Zhang et al. 2022). Given the high viscosity at the solidus, it is likely that the current speed in solid regions is extremely small and can be approximated as zero. The significant variation of viscosity below the liquidus plays a critical role in ocean dynamics. As mentioned in Section 1, this is also the reason why we choose to develop an idealized 2D model instead of employing a 3D ocean GCM.

To simplify, silicate viscosity can be regarded as a function of temperature following an exponential decay. Between the solidus and liquidus, it increases rapidly with decreasing temperature following a hyperbolic tangent (tanh) function (Figure 2(c)). For example, vertical viscosity is expressed as

$$A_z = \begin{cases} A_{z\mathrm{sol}} \cdot e^{-\frac{T - T_{\mathrm{sol}}}{T}}, & T < T_{\mathrm{sol}} \\ A_{z\mathrm{sol}} \cdot \tanh\left(a - (a - b)\dfrac{T - T_{\mathrm{sol}}}{T_{\mathrm{liq}} - T_{\mathrm{sol}}}\right), & T_{\mathrm{sol}} \leqslant T < T_{\mathrm{liq}}, \\ A_{z\mathrm{liq}} \cdot e^{-\frac{T - T_{\mathrm{liq}}}{T}}, & T \geqslant T_{\mathrm{liq}} \end{cases} \tag{11}$$

where $A_{z\mathrm{sol}}$ and $A_{z\mathrm{liq}}$ are the vertical viscosity at the solidus and liquidus, respectively; and both a and b are constants satisfying $\tanh(a) = 1$ and $b = \tanh(\frac{A_{z\mathrm{liq}}}{A_{z\mathrm{sol}}})$, respectively, ensuring a continuous change in viscosity with temperature at different temperature ranges. By default, $A_{z\mathrm{sol}} = 10^8$ and $A_{z\mathrm{liq}} = 10^1\,\mathrm{m^2\,s^{-1}}$. Similarly, the variation of horizontal viscosity with temperature follows Equation (11) with $A_{h\mathrm{sol}} = 10^8$ and $A_{h\mathrm{liq}} = 10^4\,\mathrm{m^2\,s^{-1}}$. Between the solidus and liquidus, the strict relationship between the viscosity of partially molten silicates and the melt fraction is not well considered (J. Monteux et al. 2016; Y. Zhang et al. 2022). Under the tanh function (Equation (11)), zonal velocity of partially molten silicates decreases significantly when the temperature falls below 1900 K (Section 3). For simplicity, the liquidus is directly used to determine the magma ocean boundary. Note that a solid network may be compacted at the bottom of the magma ocean under high gravity, leading to the result that the silicate viscosity can be increased by tens of orders of magnitude when the temperature just falls below the liquidus (V. Solomatov 2007). Under this circumstance, the velocity will decrease significantly when the temperature just falls below 2000 K, which may result in a relatively shallower magma ocean.

The horizontal and vertical viscosities at the solidus are lower than the realistic values ($\sim 10^{18}\,\mathrm{m^2\,s^{-1}}$; Y. Zhang et al. 2022), due to computational efficiency. Nonetheless, this modification does not influence the simulation results within the ocean, as long as the viscosity below the solidus sufficiently reduces velocity to nearly zero. The horizontal and vertical viscosities at the liquidus are considerably higher than the molecular viscosity of silicate melts ($\sim 10^{-4}\,\mathrm{m^2\,s^{-1}}$; Y. Zhang et al. 2022). In addition, the horizontal viscosity exceeds the vertical viscosity by three orders of magnitude. These values of viscosity at the liquidus are chosen for two primary reasons. First, the viscosity of silicate melts should be dominated by eddy viscosity rather than molecular viscosity in the presence of circulations and turbulences (Q. Li et al. 2017; A. Sentchev et al. 2023; C. Luo et al. 2023). Generally, the horizontal eddy viscosity is higher than the vertical eddy viscosity, given that the horizontal scale is much larger than the vertical scale (L. Prandtl 1925; T. Von Karman 1930; M. Heisel et al. 2020). Second, numerical simulations require a minimum viscosity threshold for stability. Due to the absence of the Coriolis force in our 2D model, current speed will increase rapidly with decreasing viscosity. At the molecular viscosity level, the current speed may exceed tens of meters per second, destabilizing the 2D model.

Similar to silicate viscosity, the molecular diffusivity of molten silicates also depends on pressure and temperature roughly following the Arrhenius relation (B. Gibert et al. 2003; D. B. Ghosh & B. B. Karki 2011; H. Ni et al. 2015). For simplicity, the influence of pressure on molecular diffusivity is relatively limited and can be neglected. The molecular diffusivity of molten silicates can vary from 10^{-9} to $10^{-8}\,\mathrm{m^2\,s^{-1}}$ as the temperature increases from 2000 to 3000 K (D. B. Ghosh & B. B. Karki 2011). In contrast, the molecular diffusivity of solid silicates is significantly smaller, sometimes reaching values as low as $10^{-20}\,\mathrm{m^2\,s^{-1}}$ for certain chemical compositions (Y. Zhang 2010; H. Ni et al. 2015). However, eddy diffusions within the ocean, generated by wave breaking, winds, and tides, are more important. In Earth's oceans, horizontal and vertical eddy diffusivities typically range from 10^2 to $10^4\,\mathrm{m^2\,s^{-1}}$ (S. T. Cole et al. 2015) and from 10^{-5} to $10^{-3}\,\mathrm{m^2\,s^{-1}}$ (W. Munk & C. Wunsch 1998; A. F. Waterhouse et al. 2014), respectively. These values are significantly higher than molecular diffusivity of seawater (10^{-7} to $10^{-6}\,\mathrm{m^2\,s^{-1}}$; C. Wunsch & R. Ferrari 2004). Similar to Earth, we assume that eddy diffusivity dominates diffusion within the ocean, and constant values are used. By default, $k_h = 10^3\,\mathrm{m^2\,s^{-1}}$ and $k_z = 10^{-4}\,\mathrm{m^2\,s^{-1}}$.

Beyond the ocean, diffusivity should be dominated by molecular diffusivity, which is significantly lower than that within the ocean. In our simulations, however, both horizontal and vertical diffusivities are globally uniform for two reasons. First, variable diffusivity over time and space can easily lead to numerical instability due to the limitations of the 2D model. Second, the time required for the system to reach equilibrium is inversely related to the magnitude of diffusivity. Using an extremely low diffusivity would greatly extend the time needed to attain equilibrium (Appendix). Under this approximation, horizontal diffusivity is greater than vertical diffusivity by several orders of magnitude even outside the ocean. This significant difference is partially responsible for the non-constant vertical temperature profile observed outside the ocean (see Sections 3.1 and 3.2).

2.3. External Forcings

The ocean model has not been coupled to the atmosphere but has been forced by surface temperature and wind stress, F_θ and F_u. Surface temperature (equal to potential temperature at the surface) is restored to a prescribed distribution, θ^* (Figure 2(b)), with a relaxation timescale (τ_θ) of 10 Earth days,

$$F_\theta = -\frac{1}{\tau_\theta}(\theta - \theta^*). \tag{12}$$

For example, in the eastern hemisphere, θ^* follows the local radiative balance from 0° to 85° (A. Leger et al. 2011; T. Castan & K. Menou 2011), and the substellar temperature of Kepler-10b is adopted ($T_{\text{sub}} = 3000$ K; N. M. Batalha et al. 2011); between 85° and 110°, θ^* decreases linearly with the angle away from the substellar point to 50 K (induced by the possible geothermal heating of 0.5 W m^{-2} on the nightside; A. Leger et al. 2011). Regions beyond 110° are not resolved, in which magma ocean will not form.

Zonal wind forcing is given as

$$F_u = \frac{\tau_x}{\rho_c \Delta z_s}, \tag{13}$$

where τ_x is the zonal wind stress and Δz_s is the depth of the surface layer. Following A. P. Ingersoll et al. (1985), zonal wind stress on lava worlds can be given as $\tau_x = \rho_a \omega_a V$, where ρ_a is the atmospheric density in the boundary layer, V is the atmospheric wind speed, and ω_a is the momentum transfer coefficient between surface and atmosphere. Parameter ω_a is given by

$$\omega_a = \begin{cases} \dfrac{V_e^2 - 2V_d V_e + 2V_d^2}{-V_e + 2V_d}, & V_e < 0 \\ \dfrac{2V_d^2}{V_e + 2V_d}, & V_e \geqslant 0, \end{cases} \tag{14}$$

where $V_e = \dfrac{mE}{\rho_a}$, which represents the contribution of the mean flow advection normal to the surface on the momentum exchange, where E is the evaporation rate and m is the mass per molecule; and $V_d = \dfrac{V_*^2}{V} + C_d V$, which represents the contribution of the turbulent eddies on the momentum transfer, where V_* is the friction velocity and C_d is the surface drag coefficient. The atmospheric wind speed, density, temperature, and evaporation rate of Kepler-10b with a SiO atmosphere are adopted (W. Kang et al. 2021). With strong wind speed on lava planets (~2000 m s^{-1}), C_d is taken as 10^{-2}, which is slightly higher than the estimate on Earth (~2×10^{-3} under wind speed of 40 m s^{-1}; A. Sterl 2017; W. Jiang et al. 2021). Figure 2(d) shows that the zonal wind stress is zero at the substellar point and reaches its peak, around ±100 N m^{-2}, at approximately ±40°. Note that the possible amplitude of zonal wind stress on lava planets is ~1000 times greater than that on Earth (~0.1 N m^{-2}; C. M. Risien & D. B. Chelton 2008).

2.4. Experimental Designs and Numerical Schemes

In the control simulation, only thermal forcing is included (Figure 2(b)). The planetary parameters (including planet radius and gravity) of Kepler-10b are adopted (X. Dumusque et al. 2014). The planetary and oceanic parameters for the control experiment are summarized in Table 1. Cases with both thermal and wind forcings included are also examined (Figure 2(b) and (d)). Note that, due to the influence of strong wind stress, the simulation becomes unstable when the default value of vertical viscosity (10^1 m^2 s^{-1}) is employed. Thus, for the simulations with strong wind forcing included, vertical viscosity at the liquidus is set to 10^2 m^2 s^{-1}. By default, a 5 km deep and flat-bottomed depth is adopted.

Table 1
Planetary and Oceanic Parameters in the Control Experiment

Parameter	Value	Units
Planet radius (a)	9000	km
Vertical depth (H)	5000	m
Planet gravity (g)	22	m s^{-2}
Thermal expansion coefficient (α)	2×10^{-4}	K^{-1}
Heat capacity at constant pressure (c_p)	1800	J kg^{-1} K^{-1}
Density contrast ($\Delta\rho$)	10%	
Substellar temperature (T_{sub})	3000	K
Solidus (T_{sol})	1700	K
Liquidus (T_{liq})	2000	K
Horizontal and vertical viscosities at solidus	10^8, 10^8	m^2 s^{-1}
Horizontal and vertical viscosities at liquidus	10^4, 10^1	m^2 s^{-1}
Horizontal diffusivity (k_h)	10^3	m^2 s^{-1}
Vertical diffusivity (k_z)	10^{-4}	m^2 s^{-1}

The horizontal resolution is set to 2°.2 (360 km). Vertically, we use 49 unequally spaced levels, and the vertical resolution varies nonlinearly from 40 m at the surface to 400 m at the bottom layer. At the surface layer, vertical velocity is determined by the evolution of SSH over time ($\frac{\partial\eta}{\partial t}$), which becomes zero when the system reaches equilibrium. At the bottom layer, vertical velocity is set to zero, and zonal velocity is strongly damped to zero using a linear drag with a coefficient of 10^3 s^{-1}. A no-flux boundary condition is used for temperature there. The differential equations are solved using the finite-difference method (F. Mesinger & A. Arakawa 1976). In space discretization, a centered difference method with second-order accuracy is used. For simplicity, all variables are written on the same grids, and staggered grids (F. Mesinger & A. Arakawa 1976) are not employed. In time differentiation, a backward implicit scheme is used to solve the viscosity terms of Equation (1) for numerical stability. For the remaining terms of Equation (1) and all terms in Equations (2) and (4), a forward explicit scheme is employed.

All simulations are initialized from a state of rest and a solid phase (Figure 3). The initial temperature is set to closely resemble the temperature structure dominated by vertical diffusion. Specifically, in areas where the surface temperature falls below the solidus (1700 K), the initial interior temperature is set to be equal to the surface temperature. Meanwhile, in regions where the surface temperature surpasses the solidus, both the surface and interior temperatures are set to the solidus. Notably, the equilibrated results of simulations are independent of the initial states.

3. Results

3.1. Ocean Circulation under Thermal Forcing

Magma ocean depth in the presence of thermal-driven overturning circulation is only several hundreds of meters deep (Figure 4). Initialized with a completely solid state and driven by thermal forcing, the system reaches statistical equilibrium after ~600 yr of integration (Figure A1(a)–(c)). Surface temperature, determined by the thermal forcing shown in Figure 2(b), decreases from 3000 K at the substellar point to 50 K at ±110°. Silicates start to melt at around ±84° with a

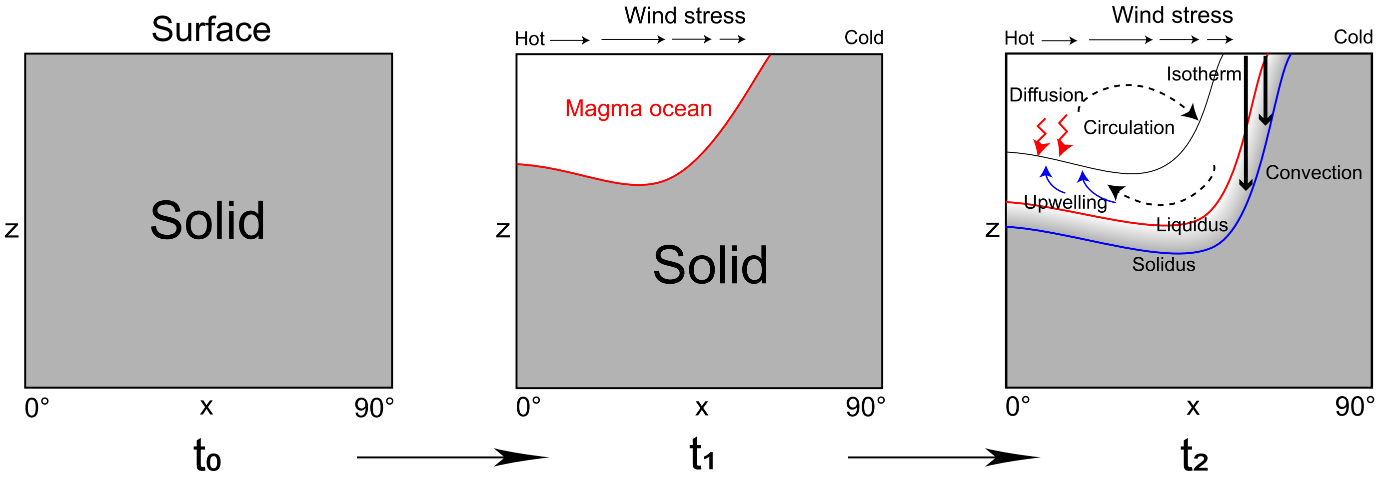

Figure 3. Schematics of the evolution of magma ocean under thermal and wind forcings. Here t_0, t_1, t_2 correspond to the initial state, the intermediate state, and the final equilibrium state, respectively. The determination processes of magma ocean depth are shown in the equilibrium state.

temperature of 1700 K (solidus) and become fully molten at about ±77° with a temperature of 2000 K (liquidus) (Figure 4(a)). The region within −77° to 77° represents the surface magma ocean. Below the surface, vertical diffusion gradually diffuses heat downward, increasing the interior temperature and melting the silicates (Figure 3).

Near the ocean edges, the temperature is nearly vertically uniform within the magma ocean. This arises from the narrow and intense vertical convection in that region (contours in Figure 4(c)), induced by the relatively low temperature and high density. Silicates sink from the surface boundary, filling the bottom layer and equalizing the temperature at the bottom layer to that at the surface edges of the ocean (Figure 4(a)). This phenomenon is similar to Earth's oceans,[5] in which the potential temperature in the deep ocean is determined by the surface temperature at high latitudes (Figure 5(c); G. K. Vallis 2019). To compensate the strong downwelling motions near the edges, a wide range of weak upwelling motions occur around the substellar region. To pump the dense fluid back up to the surface consumes energy, which is provided by vertical diffusion. The magma ocean reaches a steady state when the downward diffusion and upwelling motion balance with each other (right panel of Figure 3). The stabilized magma ocean is bowl shaped, with a maximum depth of ∼760 m at the substellar point (the black line in Figure 4(a)).

Beneath the magma ocean basin ($T < T_{\mathrm{liq}}$), the temperature remains nearly vertically constant, due to the dominant role of vertical diffusion. The small deviation from a vertically uniform temperature profile arises from the weak but nonzero circulation there (zonal velocity u ranges from 10^{-7} to $10^{-4}\,\mathrm{m\,s^{-1}}$; figures not shown). Consequently, the thermal structure is governed by a balance between horizontal advection (horizontal diffusion) and vertical diffusion in regions with relatively large (small) velocity (for more details, refer to the Appendix). In particular, in solid regions with relatively large velocities, the interior temperature is underestimated owing to horizontal advection (Figure 5(a)). In contrast, in solid regions with relatively small velocities, the interior temperature is overestimated owing to horizontal diffusion (the blue line of Figure 5(a)).

It is noteworthy that the nonconstant vertical temperature profile outside the magma ocean results from the numerical limitations of our 2D model. First, we adopt an eddy diffusivity both horizontally and vertically, i.e., the horizontal diffusivity is significantly larger than the vertical diffusivity (Table 1). Second, the viscosity utilized below the solidus ($10^{8}\,\mathrm{m^2\,s^{-1}}$) is still significantly smaller than the realistic viscosity of solid silicates ($\sim 10^{18}\,\mathrm{m^2\,s^{-1}}$; Section 2.2). Note that the interior temperature beyond the magma ocean might have not reached equilibrium owing to the long timescales involved (Appendix). Despite this, the temperature beyond the magma ocean remains lower than the liquidus, which will not affect the above magma ocean.

Silicate density is determined by temperature and pressure (Equation (10) and Figure 2(a)), and the influence of pressure is limited owing to the shallow depths. Thus, silicate density follows a similar pattern to temperature, i.e., density is larger in the regions where temperature is low and is smaller in the regions where temperature is high (Figure 4(b)). Note that there is a 10% change in density from the solidus to the liquidus, which results in the largest density gradient near the phase transition regions.

In our 2D model without planetary rotation, zonal currents are primarily driven by zonal pressure gradient force and balanced by vertical viscosity (left panels of Figure A2). Near the surface, the zonal pressure gradient force, dominated by SSH gradient (Equation (7)), is positive (negative) on the east (west) of the substellar point (Figure 4(d)). Thus, zonal currents near the surface flow outward from the substellar point, reaching a maximum value of $\sim 0.1\ \mathrm{m\,s^{-1}}$ (colors in Figure 4(c)). In the interior ocean, the zonal pressure gradient force, dominated by the interior density gradient (Equation (7)), is negative (positive) on the east (west) of the substellar point. Thus, interior zonal currents flow toward the substellar point. A clockwise (anticlockwise) overturning circulation occurs on the east (west) of the substellar point, with upwelling motions around the substellar region and downwelling motions near the ocean edge (contours in Figure 4(c)). Outside the ocean, ocean currents become weak owing to the strong viscosity below the liquidus.

---

[5] The long-term mean potential temperature data of Earth are from the NCEP Global Ocean Data Assimilation System (GODAS; https://psl.noaa.gov/data/gridded/data.godas.html).

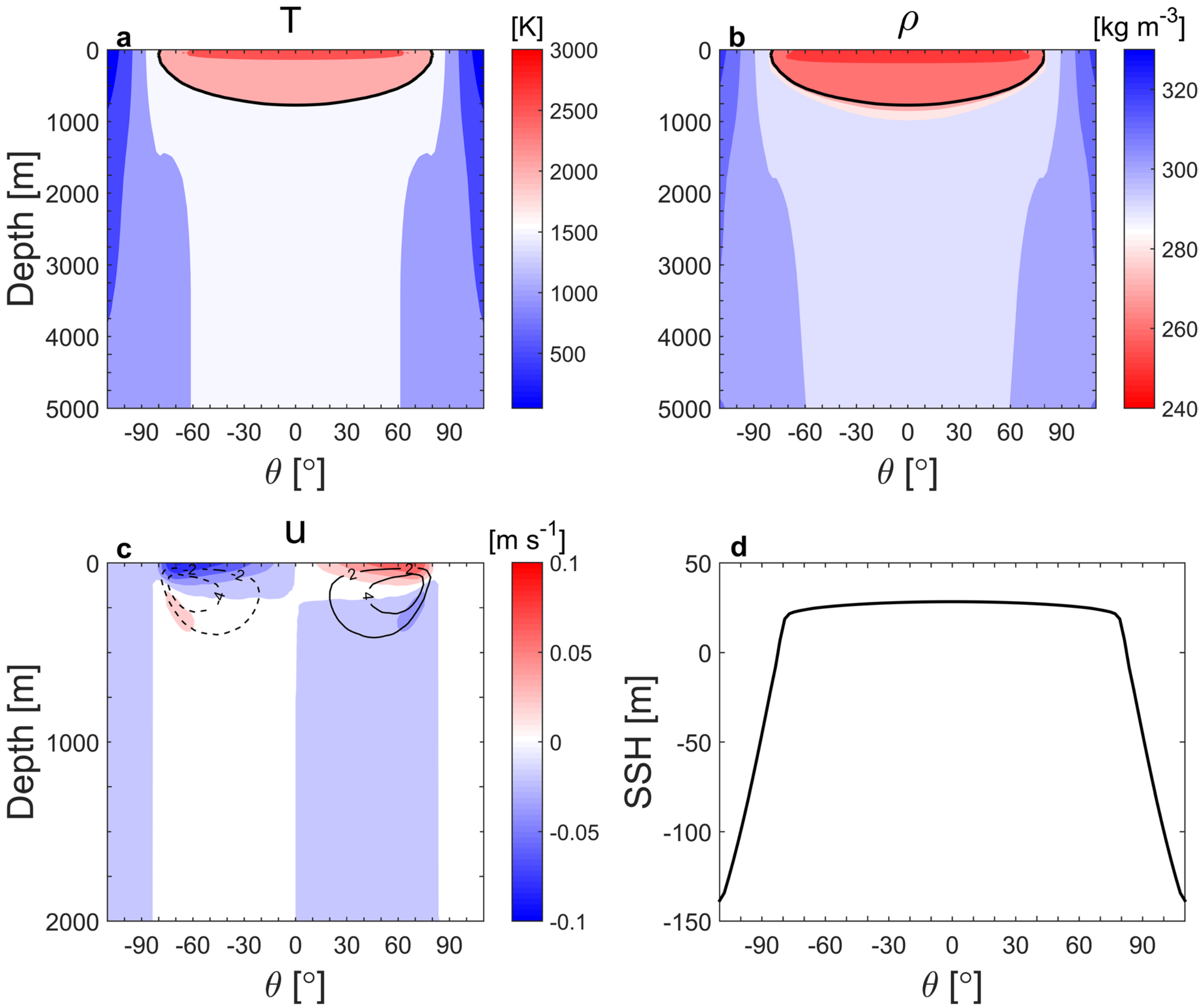

Figure 4. Snapshot results of the simulation with thermal forcing only. (a) Temperature (T) in K, (b) density (ρ) in kg m^{-3}, (c) zonal current speed (u) in m s^{-1} (colors) and velocity stream function (ψ) in m^2 s^{-1} (contours) with an interval of 2.0 m^2 s^{-1} and (d) SSH in m. The black solid lines in panels (a) and (b) indicate the location of the magma ocean boundary, which is determined by the liquidus. Solid lines in panel (c) correspond to positive values (a clockwise overturning circulation), and dashed lines correspond to negative values (an anticlockwise overturning circulation). As the ocean circulation is confined to the upper ∼1 km, panel (c) shows only the zonal velocity within the upper 2 km.

SSH is positive within the magma ocean, reaching a maximum value of 30 m at the substellar point and gradually decreasing away from it, attaining a minimum value of −140 m at ±110° (Figure 4(d)). As mentioned above, surface heat is gradually diffused downward over time, leading to an increase in the vertical-mean temperature and then a continuous rise in SSH within the ocean (Figure A1(c)), due to thermal expansion. This corresponds to a persistent convergence of the vertical integral of zonal velocity within the ocean before the system reaches equilibrium (Equation (4)). Conversely, outside the magma ocean, SSH experiences a continuous decrease, becoming increasingly negative (Figure A1(c)). This corresponds to a continuous divergence of the vertical integral of zonal velocity before reaching equilibrium.

3.2. Ocean Circulation under Both Thermal and Wind Forcings

Magma ocean depth remains several hundreds of meters deep, even with both thermal and wind forcings (Figure 6). The system reaches a dynamic equilibrium after ∼600 yr of integration (Figures A1(d)–(f)). The temperature field closely resembles that under thermal forcing alone (Figure 6(a)). In contrast, the ocean overturning circulation is primarily dominated by wind forcing. There are strong upwelling motions around ±30° and downwelling motions around ±55° induced by the divergence and convergence of zonal currents near the surface, respectively (Figure 6(c)). With the effect of wind stress, magma ocean becomes relatively shallower around the substellar region and relatively deeper around ±40° (Figure 3). The magma ocean reaches its deepest depth of 960 m at ±35° (the black line in Figure 6(a)). The vertical temperature profiles under both thermal and wind forcings remain similar to those under thermal forcing only (Figure 5(b)).The density pattern closely follows the temperature field and is primarily determined by temperature (Figure 6(b)).

In the presence of strong wind forcing, surface zonal currents are primarily driven by the zonal wind stress, which is balanced by vertical viscosity and the zonal pressure gradient force (right panels of Figure A2). As a result, zonal currents align with the

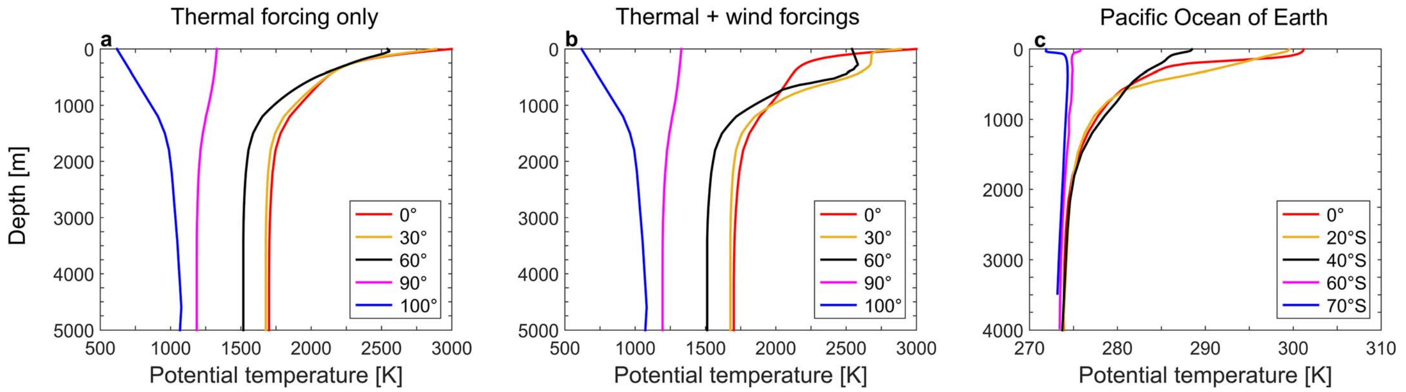

Figure 5. Comparison of vertical temperature profiles of this study with those in Earth's oceans. (a, b) Vertical temperature profiles at varying angles away from the substellar point under thermal forcing only and under both thermal and wind forcings, respectively. (c) Vertical potential temperature profiles in the North Pacific of Earth at varying latitudes at 170° west.

direction of zonal wind stress near the surface, flowing outward from the substellar point (Figure 2(d) and colors in Figure 6(c)). The currents reach a maximum velocity of $1.0\ \mathrm{m\ s^{-1}}$ at approximately ±40°, where the zonal wind stress is strongest. Below the surface layer, the contributions of SSH gradient and density gradient on the zonal pressure gradient are in the same direction, driving zonal currents toward the substellar point. To satisfy mass continuity, there is upwelling motion near ±30° and downwelling motion near ±55°. Thus, a clockwise (anticlockwise) overturning circulation forms on the east (west) side of the substellar point (contours in Figure 6(c)).

SSH is immediately influenced by the imposed wind stress when the simulation starts. Thus, at the beginning of the simulation, SSH is extremely low around the substellar region owing to the divergence of wind stress, and vice versa (Figure A1(f)). As the magma ocean reaches deeper over time, SSH continuously increases owing to thermal expansion, and vice versa outside the ocean. In the final equilibrated state, SSH exhibits a local minimum value of 15 m at the substellar point and a local maximum value of 45 m at around ±60° (Figure 6(d)).

3.3. Comparisons with Previous Studies

Magma ocean depth determined by ocean circulation is much shallower than that determined by adiabats (Figure 1). As in our study, when the interior heat source is weak or absent, the interior temperature is determined by stellar heating and ocean circulation. Along the magma ocean edge, fluid cools and sinks to the bottom, releasing gravity potential energy. To pump this dense fluid back up to the surface consumes energy, which is provided by vertical diffusion. In the upwelling regions near the substellar point, the downward diffusive heat flux needs to balance the upward advective heat flux, leading to the so-called advective−diffusive balance (Appendix; E. S. Kite et al. 2016; G. K. Vallis 2019)

$$w\frac{\partial T}{\partial z} \approx \frac{\partial}{\partial z}\left(k_z\frac{\partial T}{\partial z}\right). \tag{15}$$

Thus, the vertical temperature profile within the magma ocean can be given as

$$T(z) = T_b + (T_s - T_b)e^{z/\mathcal{D}},\ \mathcal{D} = k_z/w, \tag{16}$$

where T_s and T_b represent the surface temperature and bottom temperature of the magma ocean, respectively, and $\mathcal{D}$ represents the characteristic scale for the thermocline depth, determined by the ratio of vertical diffusivity (k_z) to the upwelling velocity (w). In this study, the magma ocean boundary is determined by the liquids, i.e., $T_b = T_{\mathrm{liq}}$. Furthermore, we assume that the magma ocean depth is comparable to the thermocline depth (E. S. Kite et al. 2016). In the case of thermal forcing only (Figure 4), with $k_z \sim 10^{-4}\ \mathrm{m^2\ s^{-1}}$ and $w \sim 3 \times 10^{-7}\ \mathrm{m\ s^{-1}}$ within the magma ocean, the calculated thermocline depth is ∼300 m, being comparable to that obtained from the simulations.

In scenarios when wind forcing dominates thermal forcing, the temperature profile deviates from advection–diffusion balance and is instead governed by horizontal and vertical advection (Appendix; G. K. Vallis 2019)

$$u\frac{\partial T}{\partial x} + w\frac{\partial T}{\partial z} \approx 0,\ \mathcal{D}' = \frac{wL}{u}, \tag{17}$$

where $\mathcal{D}'$ represents the characteristic scale for the thermocline depth in the wind-forcing-dominated scenario and L represents the horizontal scale for the magma ocean. In the simulation with both thermal and wind forcings (Figure 6), where $L \sim 10^7$ m, $u \sim 1.0\ \mathrm{m\ s^{-1}}$, and $w \sim 5 \times 10^{-5}\ \mathrm{m\ s^{-1}}$ within the magma ocean, the calculated thermocline depth is ∼500 m, aligning reasonably well with the results obtained from simulations.

Strictly speaking, the velocities utilized in Equations (16) and (17) are intricately influenced by external forcings and various parameters, encompassing viscosity, diffusivity, gravity, and thermal expansion coefficients, among others. However, for the sake of simplicity, we offer an estimation of magma ocean depth employing the zonal and vertical velocities derived from numerical simulations. Referring to the theories in Earth's oceans (G. K. Vallis 2019), E. S. Kite et al. (2016) provided scaling laws for horizontal velocity and magma ocean depth in scenarios dominated by thermal forcing. Nonetheless, their scaling analyses overlook the substantial impact of wind forcing. In Paper II of this series, we will provide the dependences of both current speed and ocean depth on external forcings and diverse parameters across various dynamical regimes and forcing scenarios.

Magma ocean depth derived from our 2D model demonstrates a notable alignment with estimations derived from a geostrophic balance system (i.e., the pressure gradient force is balanced by the Coriolis force) by E. S. Kite et al. (2016). Their scaling analysis indicated that the magma ocean depth in a

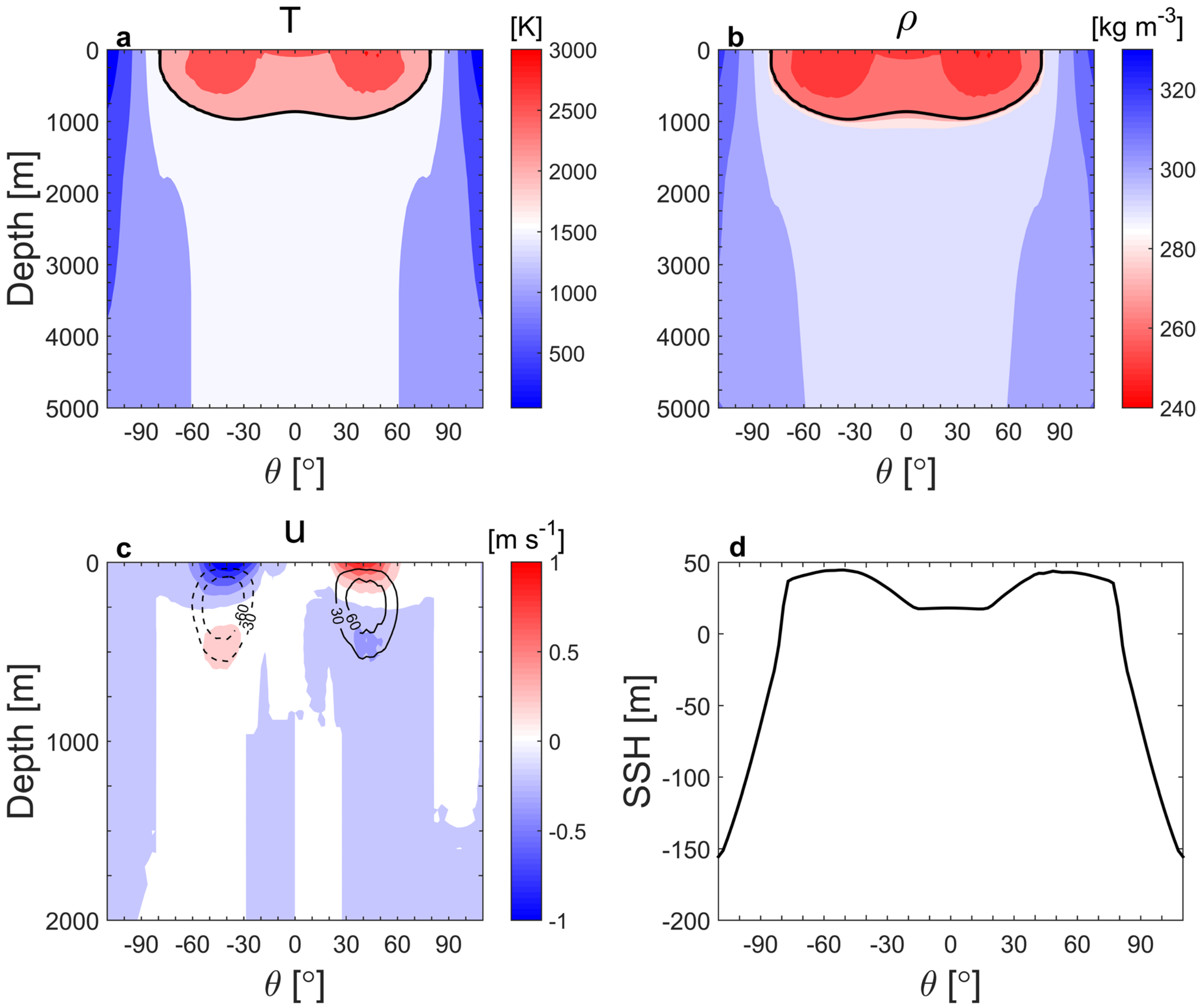

Figure 6. Same as Figure 4, except that both thermal and wind forcings are included and $A_z = 10^2\ \mathrm{m^2\ s^{-1}}$ at the liquidus in this simulation. The interval of the velocity stream function is 30.0 $\mathrm{m^2\ s^{-1}}$ in the contours of panel (c).

geostrophic balance system is over 100 times shallower compared to scenarios without ocean circulation. In our 2D model, however, the zonal momentum is in balance between the vertical viscosity term and the pressure gradient force (Figure A2). The consistency in magma ocean depth between models operating within varying dynamical regimes reinforces the pivotal influence of ocean circulation in modulating magma ocean depths. For a more comprehensive elucidation and comparative analysis across different dynamical regimes, please refer to Paper II of this series.

3.4. *Implications for Observations*

E. S. Kite et al. (2016) estimated the ocean heat transport (OHT) divergence due to thermal-driven overturning circulation on lava planets. Using simple scalings based on 3D equations, they suggested an oceanic current speed of $10^{-2}\ \mathrm{m\ s^{-1}}$ and a magma ocean depth of $\mathcal{O}(100)$ m (consistent with Figure 4). Consequently, their calculated OHT divergence was approximately four orders of magnitude lower than the stellar insolation ($\sim 10^6\ \mathrm{W\ m^{-2}}$; Figure 7(c)). A. Leger et al. (2011) also provided an estimation for OHT divergence on CoRoT-7b. In contrast to the geostrophic balance system, they considered zonal current speed without the Coriolis force and attained a maximum value of $\sim 2\ \mathrm{m\ s^{-1}}$. With an ocean depth of 100 m, they suggested an OHT convergence of $10^4\ \mathrm{W\ m^{-2}}$, still two orders of magnitude smaller than the stellar insolation.

Here the OHT divergence of numerical simulations with thermal forcing alone and with both thermal and wind forcings is shown in Figure 7. If the velocity were entirely zero in solid regions, there would be no OHT. Thus, only the OHT divergence within the magma ocean is calculated. For comparison, the stellar insolations of four different tidally locked lava planets are presented in Figure 7(c). In the case of thermal forcing alone (Figure 7(a)), OHT diverges within about ±50° and converges outside ±50°. The OHT divergence/convergence reaches a maximum value of $\sim 10^4\ \mathrm{W\ m^{-2}}$ under a substellar temperature of 3000 K, nearly two orders of magnitude lower than the stellar insolation (Figure 7(c)). With both thermal and wind forcings (Figure 7(b)), the OHT divergence/convergence reaches a maximum value of $2 \times 10^5\ \mathrm{W\ m^{-2}}$, remaining smaller than the stellar insolation.

To quantify the effects of ocean circulation on surface temperature, we estimate the ocean temperature anomaly (T')

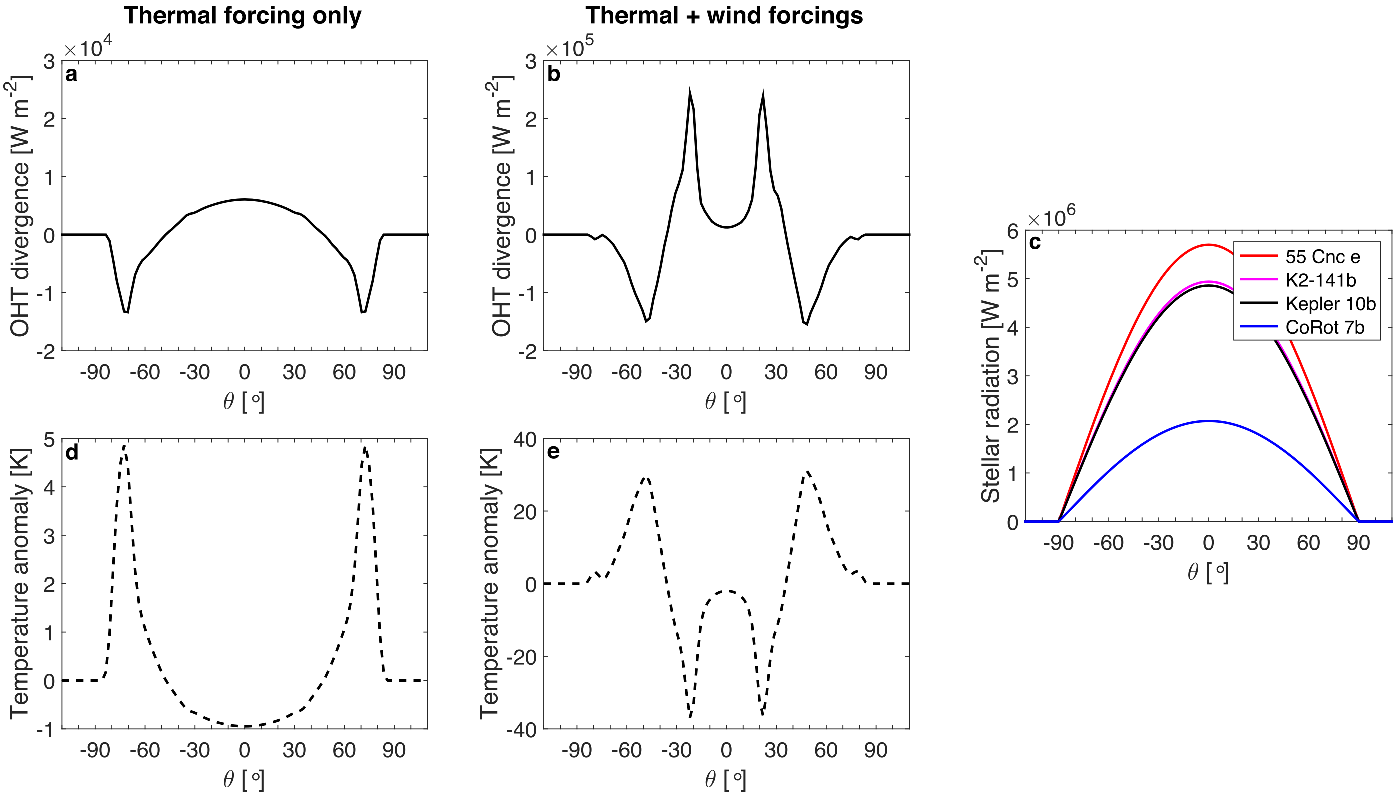

Figure 7. The OHT divergence ($F_o = \frac{\partial}{\partial x}\int_{-\mathcal{D}}^{0} c_p \rho u T dz$) (panels (a) and (b)) and temperature anomaly induced by ocean circulation (panels (d) and (e)) under thermal forcing only (left panels) and under both thermal and wind forcings (middle panels). Note that positive values of OHT divergence correspond to heat loss and negative values of OHT divergence correspond to heat gain. Results shown in the left and middle panels are based on the simulation results shown in Figures 4 and 6, respectively. The stellar insolation of different lava planets is shown for comparison (panel (c)).

induced by ocean circulation using the following formula:

$$T' = \begin{cases} \left(\dfrac{S - F_o}{\sigma_b}\right)^{\frac{1}{4}} - \left(\dfrac{S}{\sigma_b}\right)^{\frac{1}{4}}, & S \geqslant F_o \\ -\left(\dfrac{F_o - S}{\sigma_b}\right)^{\frac{1}{4}} - \left(\dfrac{S}{\sigma_b}\right)^{\frac{1}{4}}, & S < F_o \end{cases}, \qquad (18)$$

where S represents stellar insolation, F_o represents the OHT divergence, and σ_b represents the Stefan–Boltzmann constant. It should be noted that positive values of F_o correspond to heat loss, leading to a negative temperature anomaly, while negative values of F_o correspond to heat gain, resulting in a positive temperature anomaly. In the case of thermal forcing alone, the temperature anomaly (T') induced by ocean circulation ranges from -1 to 5 K (Figure 7(d)). In particular, the ocean circulation decreases the temperature within ±50° while increasing the temperature around ±70°. When both thermal and wind forcings are imposed, T' ranges from -40 to 20 K (Figure 7(e)). Specifically, the ocean circulation decreases (increases) the temperature around ±20° (±50°). Generally speaking, the ocean circulation tends to reduce the horizontal temperature gradient within the magma ocean. However, the temperature anomaly remains significantly lower than the radiative equilibrium temperature. Consequently, the impact of oceanic overturning circulation on surface temperature, and thus on the thermal phase curve, is limited.

The OHT divergence increases with the intensity of stellar insolation. As the stellar radiation intensifies, both the substellar temperature and the horizontal scale of the magma ocean increase, leading to stronger ocean circulation and deeper magma ocean. Consequently, the OHT divergence escalates. However, even under varying intensities of stellar radiation, the OHT divergence remains two orders of magnitude smaller than the stellar insolation. For further insights, we delve into detailed numerical and theoretical analyses in Paper II of this series.

4. Discussions

4.1. Influence of Latent Heat

The ocean model has not been coupled with the atmosphere. Surface temperature is completely determined by local radiative balance (A. Léger et al. 2009). As mentioned in Section 1, atmospheric latent heat is much smaller than the stellar insolation (T. Castan & K. Menou 2011; E. S. Kite et al. 2016). This assumption seems to work for an evaporation-driven atmosphere (A. P. Ingersoll et al. 1985).

4.2. Influence of Molecular Diffusivity

The variation of silicate diffusivity with temperature is not included in our 2D model. Basically, silicate molecular diffusivity can vary approximately from 10^{-20} to 10^{-8} m^2 s^{-1} from solid to liquid states (Section 2.2). In our 2D model, a constant and globally uniform eddy diffusivity is employed for simplicity, which is significantly larger than the molecular diffusivity. Outside the magma ocean, the temperature is governed by vertical diffusion. Thus, the magnitude of diffusivity will not exert an evident influence on the thermal structure, which will primarily affect the equilibrium time (Appendix). However, the significant difference between the horizontal diffusivity and vertical diffusivity allows the horizontal diffusion to play a role in affecting the thermal structure in solid regions (Sections 3.1 and 3.2).

4.3. Influence of Planetary Rotation

The 2D model does not account for the Coriolis force. The significance of planetary rotation can be evaluated using the Rossby number ($R_o = \frac{u}{\Omega L}$, where L is the typical scale of the horizontal range of the magma ocean and Ω is the planetary rotation rate) and the Ekman number ($E_z = \frac{A_z}{\Omega D^2}$, where D is the typical scale of the vertical range of the magma ocean) (G. K. Vallis 2019). Here R_o represents the ratio of the nonlinear advection term to the Coriolis force, while E_z denotes the ratio of the vertical viscosity term to the Coriolis force.

Using the planetary rotation rate of Kepler-10b, $\Omega \approx \frac{2\pi}{(0.84\ \mathrm{days})} \sim 10^{-4}\ \mathrm{s}^{-1}$ (N. M. Batalha et al. 2011), and assuming that $L \sim 10^7$ m, $D \sim 10^3$ m, $A_z \sim 10^1\ \mathrm{m^2\ s^{-1}}$, and $u \sim 0.1\ \mathrm{m\ s^{-1}}$ for thermal-forcing-dominated simulation (Figure 4), we can calculate Rossby number $R_o \sim 5 \times 10^{-4}$ and Ekman number $E_z \sim 0.1$. Hence, both the nonlinear advection and vertical viscosity terms are significantly smaller than the Coriolis force, spanning 1–4 orders of magnitude. Consequently, if the Coriolis force were considered, the system would likely be in geostrophic balance, in which the pressure gradient force is balanced by the Coriolis force.

In Paper II of this series, we delve into a detailed discussion and comparison of the ocean circulation and ocean depth across three different dynamical regimes: viscosity-dominant, advection-dominant, and rotation-dominant regimes. Theoretical results suggest that the difference in magma ocean depth among the three dynamical regimes is relatively constrained, consistently shallower than that determined by the adiabat.

4.4. Influence of Internal Heating

Given that most tidally locked lava planets have cooled over billions of years, internal heating is not fully considered in our 2D model. In the absence of ocean circulation, the interior temperature is governed by diffusion. Without internal heating, the interior temperature should be vertically uniform. By comparison, the interior temperature gradually increases from the surface temperature with depth in the presence of internal heating. The vertical temperature gradient (γ) induced by internal heating is expressed as (A. Adcroft et al. 2001; J. R. Scott et al. 2001; J. Emile-Geay & G. Madec 2009; F. Wang et al. 2016)

$$\gamma = -\frac{\partial T}{\partial z} = \frac{Q}{\rho c_p k_z}, \tag{19}$$

where Q represents the internal heating rate and z represents the distance from the surface. Assuming an internal heating rate of $Q \sim 0.5\ \mathrm{W\ m^{-2}}$ (A. Leger et al. 2011), along with the ocean parameters presented in Table 1, the resulting vertical temperature gradient $\gamma \sim 1\ \mathrm{K\ km^{-1}}$. This implies that the temperature would increase from 3000 K at the surface to 3100 K at a depth of 100 km near the substellar point. Thus, when internal heating is weak, its effect on the magma ocean is not strong. However, when internal heating is so strong that vigorous convection occurs, magma ocean depth could be significantly increased (Figure 1(a); A. Leger et al. 2011; C.-É. Boukaré et al. 2022, 2023; T. G. Meier et al. 2023).

4.5. Surface Boundary of Magma Ocean

In this study, we assume a fixed magma ocean boundary at the sea surface, because surface temperature is fixed in the simulations. This assumption proves effective for tidally locked lava planets, where the influence of ocean circulation on both surface temperature and magma ocean boundary is negligible (Figure 7). Furthermore, we can also discern which process dominates the surface temperature by comparing the timescales of radiative equilibrium, horizontal diffusion, and horizontal advection (Equation (A2)). The radiative timescale can be estimated using the formula (A. P. Showman et al. 2010) $\tau_{\mathrm{rad}} = \frac{c_p p_s}{4 g \sigma_b T_e^3}$, where p_s denotes the atmospheric pressure and T_e denotes the radiative equilibrium temperature. For the silicate atmosphere on tidally locked lava planets (T. Castan & K. Menou 2011; T. G. Nguyen et al. 2020; W. Kang et al. 2021), assuming $c_p \sim 1800\ \mathrm{J\ kg^{-1}\ K^{-1}}$, $p_s \sim 10^4$ Pa, and $g \sim 20\ \mathrm{m\ s^{-2}}$, the radiative equilibrium timescale is ∼400 s near the magma ocean boundary ($T_e \sim 2000$ K). Given that zonal velocity is approximately $10^{-4}\ \mathrm{m\ s^{-1}}$ there (figure not shown), the timescales of both horizontal diffusion and horizontal advection are around 3000 yr (Appendix), which are considerably longer than the radiative timescale. Overall, horizontal diffusion and advection are unable to extend the magma ocean boundary beyond the day/night terminator.

4.6. Mass-driven Overturning Circulation

For a tidally locked lava planet, there is persistent evaporation (condensation) at the magma surface where the atmospheric pressure is lower (higher) than the saturated vapor pressure (T. Castan & K. Menou 2011; T. G. Nguyen et al. 2020). Therefore, there is mass loss where surface evaporates and mass gain where atmosphere condenses. For example, for a Na atmosphere on K2-141b, magma surface loses mass within about ±40° and gains mass elsewhere (T. G. Nguyen et al. 2020). The horizontal gradient in mass flux can result in a gradient in surface height and thereby in surface pressure, which then drives an overturning circulation. Different from the thermal-driven or wind-dominated circulation (Figures 4 and 6), the mass-driven circulation exhibits an opposite direction, with surface ocean currents flowing toward the substellar point (E. S. Kite et al. 2016; T. Tokano & R. D. Lorenz 2016). This mass-driven circulation is beyond the scope of our study owing to the limitations of our 2D model. And its influences on the surface energy budget and surface composition need to be addressed using a more complicated 3D ocean GCM.

5. Summary

Magma ocean can form and persist in the dayside of tidally locked lava planets, where surface temperatures are high enough to melt typical silicates under intense stellar radiation. In this study, we aim to simulate the magma ocean of tidally locked lava planets using an idealized 2D (x–z) ocean circulation model under the assumption of a small or no internal heat flux. Our main results are as follows:

(1) In the presence of thermal-driven overturning circulation, magma ocean depth is only $\mathcal{O}(100)$ m. The overturning circulation, driven by surface temperature contrast, is clockwise (anticlockwise) on the east (west) of the substellar point.
(2) The zonal wind stress can reach $\sim 100\,\mathrm{N\,m^{-2}}$, roughly 1000 times that on Earth. Under such strong wind forcing, the ocean overturning circulation intensifies. Overall, magma ocean depth under thermal and wind forcings remains $\mathcal{O}(100)$ m.
(3) Determined by ocean circulation, magma ocean depth is more than 100 times shallower than that determined by adiabats. Our simulation results are consistent with that suggested by E. S. Kite et al. (2016).
(4) The OHT divergence/convergence is 1–2 orders of magnitude smaller than the stellar radiation. Thus, the effects of ocean circulation on the climate are limited.

In Paper I of this series, we have presented simulation results for ocean circulation and ocean depth in a nonrotating, viscosity-dominant 2D system. In Paper II, we will theoretically explore ocean circulation and ocean depth in three different dynamical regimes: nonrotating viscosity-dominant, nonrotating inviscid limit, and rotation-dominant regimes. We further compare the scaling results with those from numerical simulations. The results consistently indicate that, under different mechanisms and parameters, magma ocean depth in the presence of ocean circulation remains $\mathcal{O}(100)$ m.

Acknowledgments

We express our gratitude to Feng Ding, Xinyu Wen, and Yonggang Liu for their valuable contributions and insightful discussions. J. Y. is supported by NSFC under grant Nos. 42075046, 42275134, and 42161144011. This work has been supported by the science research grants from the China Manned Space Project (No. CMS-CSST-2021-B09).

The 2D model employed in this study is developed by the authors and is available at https://github.com/YanhongLai/Two-dimensional-model-for-magma-ocean-on-lava-worlds.git. The simulation data used are archived on Zenodo: doi:10.5281/zenodo.11467142.

Appendix
Time Series and Momentum Budget

Numerical simulations approximately reach dynamical equilibrium after 600 yr of integration. For example, the time series of zonal-mean kinetic energy, temperature at the substellar point, and SSH are presented in Figure A1. Initialized from a rest state, zonal-mean kinetic energy increases over time. It reaches maximum values of about $10^{-3}\,\mathrm{m^2\,s^{-2}}$ at the surface for simulations with thermal forcing only and $0.12\,\mathrm{m^2\,s^{-2}}$ when both thermal and wind forcings are included (Figures A1(a) and (d)). Note that oscillations in the kinetic energy time series may be induced by numerical instability.

The time required for equilibrium can be estimated by simple scalings. According to Equations (1) and (2), the equilibrium time for zonal velocity (kinetic energy) and temperature can be given, respectively, as

$$\tau_u \sim \max\left\{\frac{L}{U}, \frac{H}{W}, \frac{L^2}{A_h}, \frac{H^2}{A_z}\right\}, \tag{A1}$$

$$\tau_T \sim \max\left\{\frac{L}{U}, \frac{H}{W}, \frac{L^2}{k_h}, \frac{H^2}{k_z}\right\}, \tag{A2}$$

where L and H are the horizontal and vertical scales of the simulated domain, respectively; and U and W are the

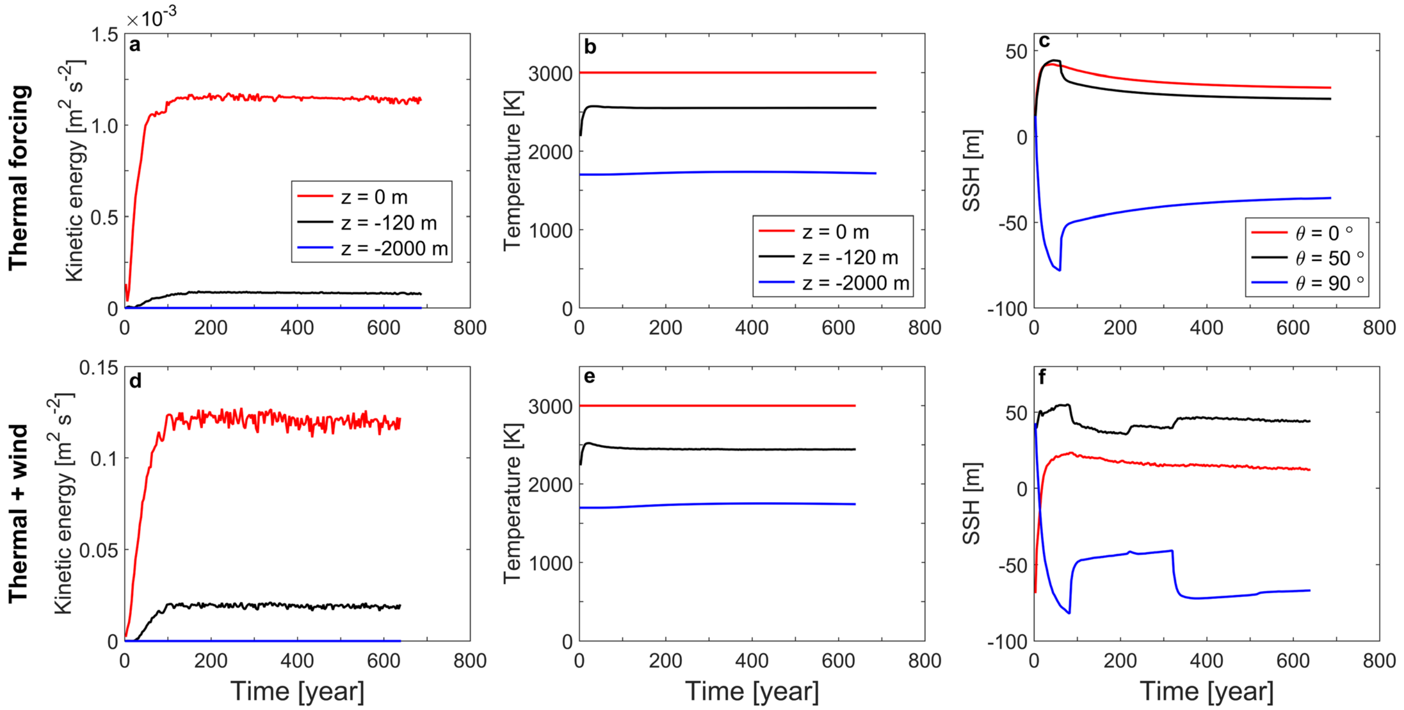

Figure A1. Time series of the simulations shown in Figure 4 (top panels) and Figure 6 (bottom panels). (a, d) Zonal-mean kinetic energy at different depths, (b, e) temperature of the substellar point at varying depths, and (c, f) SSH at different angles, as a function of time. Note that the system is initialized with a rest state.

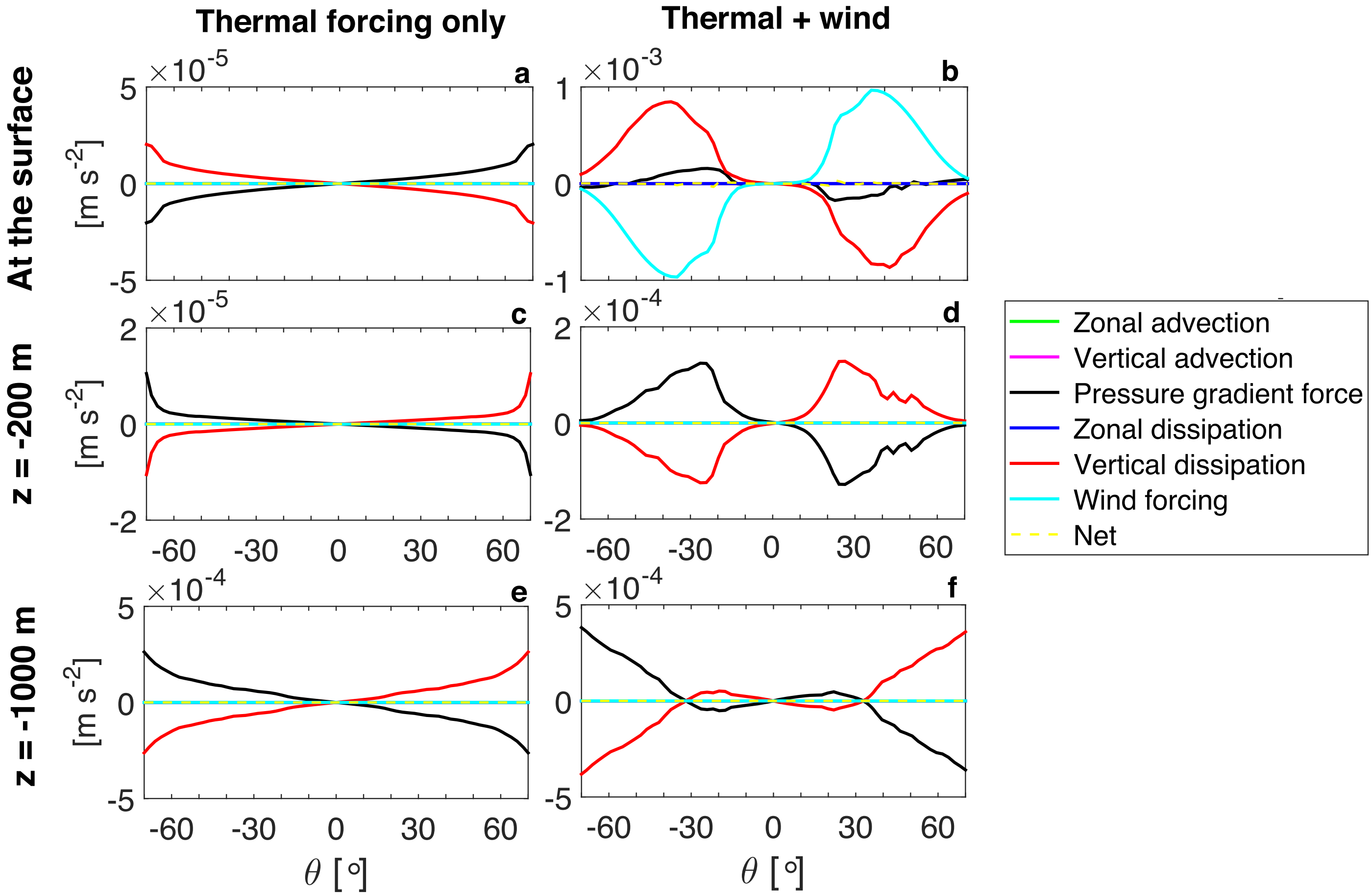

Figure A2. The zonal momentum budget at different depths of the simulations shown in Figure 4 (left panels) and Figure 6 (right panels). From top to bottom panels, they are zonal momentum budget at the surface (panels (a) and (b)), at a depth of 200 m (panels (c) and (d)), and at a depth of 1000 m (panels (e) and (f)), respectively. Due to the substantial difference in zonal momentum between the interior and exterior magma ocean, only the zonal momentum budget within ±70° is shown.

characteristic values of zonal and vertical current speeds, respectively. Given the significant difference in the viscosity and current speed within and outside the magma ocean, we estimate their timescales of each term separately.

The following estimation takes the results under both thermal and wind forcings as an example (Figure 6). Within the magma ocean, $U \sim 1.0\,\mathrm{m\,s^{-1}}$, $W \sim 5 \times 10^{-5}\,\mathrm{m\,s^{-1}}$, $A_h \sim 10^{4}\,\mathrm{m^{2}\,s^{-1}}$, $A_z \sim 10^{2}\,\mathrm{m^{2}\,s^{-1}}$, $k_h \sim 10^{3}\,\mathrm{m^{2}\,s^{-1}}$, $k_z \sim 10^{-4}\,\mathrm{m^{2}\,s^{-1}}$, $L \sim 2 \times 10^{7}\,\mathrm{m}$, and $H \sim 5 \times 10^{3}\,\mathrm{m}$, we can estimate that $\tau_u \sim 300\,\mathrm{yr}$ and $\tau_T \sim 3000\,\mathrm{yr}$, which are restricted by horizontal viscosity and horizontal diffusion, respectively. In particular, the temperature is actually dominated by horizontal and vertical advection within the magma ocean (for details, see below). Thus, the temperature within the magma ocean can reach dynamic equilibrium after ~300 yr of integration. Outside the magma ocean, we take the results in the regions where the temperature is around the solidus as an example: $U \sim 10^{-5}\,\mathrm{m\,s^{-1}}$, $W \sim 10^{-8}\,\mathrm{m\,s^{-1}}$, $A_h \sim 10^{8}\,\mathrm{m^{2}\,s^{-1}}$, $A_z \sim 10^{8}\,\mathrm{m^{2}\,s^{-1}}$, and the values of both τ_u and τ_T are ~30,000 yr, restricted by horizontal advection.

The timescales of each term in the momentum and thermal equations not only determine the time required to reach equilibrium but also play a crucial role in determining the dominant physical processes governing the ocean dynamics. Different from the equilibrium time, the ocean dynamics is governed by terms with relatively short timescales. In the zonal momentum equation, the timescale of the vertical viscosity term is consistently smallest everywhere, which dominates over the advection and horizontal viscosity terms. Thus, the ocean circulation is governed by a balance between vertical viscosity and pressure gradient force (Figure A2).

In the thermal equation, the dominant physical processes differ within and outside the magma ocean. Within the magma ocean ($T \geqslant T_{\mathrm{liq}}$), the timescales of both horizontal advection and vertical advection are approximately 0.3 yr, which are shorter than the remaining terms. Outside the magma ocean ($T < T_{\mathrm{liq}}$), U ranges from 10^{-7} to $10^{-4}\,\mathrm{m\,s^{-1}}$ and W ranges from 10^{-9} to $10^{-7}\,\mathrm{m\,s^{-1}}$. Thus, in solid regions with relatively large velocities, the timescales of horizontal advection and vertical diffusion are smallest and comparable (~3000 yr). By comparison, in solid regions with relatively small velocities, the timescales of horizontal diffusion and vertical diffusion are smallest and comparable (~3000 yr).

According to the above estimation, under both thermal and wind forcings, the thermal structure is governed by a balance between horizontal advection and vertical advection within the magma ocean. Outside the magma ocean, the thermal structure is governed by a balance between horizontal advection (horizontal diffusion) and vertical diffusion in regions with relatively large (small) velocity. It is noteworthy that under thermal forcing only (Figure 4) the thermal structure within the magma ocean is controlled by the balance between vertical advection and vertical diffusion.

In the 2D model, due to the lack of the Coriolis force, the system is not in geostrophic balance as it is in 3D models (E. S. Kite et al. 2016; G. K. Vallis 2019). Without wind forcing, zonal momentum is in balance between the zonal pressure gradient force and vertical viscosity both at the surface and in the interior ocean (left panels of Figure A2). For example, on the east of the substellar point, the zonal pressure gradient force is determined by the SSH gradient and is positive at the surface, while it is determined by the interior density gradient and is negative in the interior. Thus, zonal currents in the upper and lower ocean are in opposite directions (Figure 4(c)). In the presence of strong wind forcing, the wind forcing is balanced by the zonal pressure gradient force and vertical viscosity at the surface (Figure A2(b)). The zonal momentum remains in balance between the zonal pressure gradient force and vertical viscosity below the surface (Figures A2(d) and (f)).

ORCID iDs

Yanhong Lai https://orcid.org/0000-0001-9700-9121
Jun Yang https://orcid.org/0000-0001-6031-2485
Wanying Kang https://orcid.org/0000-0002-4615-3702

References

Adcroft, A., Scott, J. R., & Marotzke, J. 2001, GeoRL, 28, 1735
Batalha, N. M., Borucki, W. J., Bryson, S. T., et al. 2011, ApJ, 729, 27
Beichman, C. A., & Greene, T. P. 2018, arXiv:1803.03730
Boukaré, C.-É., Cowan, N. B., & Badro, J. 2022, ApJ, 936, 148
Boukaré, C.-É., Lemasquerier, D., Cowan, N., Samuel, H., & Badro, J. 2023, arXiv:2308.13614
Bourrier, V., Dumusque, X., Dorn, C., et al. 2018, A&A, 619, A1
Brinkman, C. L., Weiss, L. M., Dai, F., et al. 2023, AJ, 165, 88
Castan, T., & Menou, K. 2011, ApJL, 743, L36
Chao, K.-H., deGraffenried, R., Lach, M., et al. 2021, ChEG, 81, 125735
Cole, S. T., Wortham, C., Kunze, E., & Owens, W. B. 2015, GeoRL, 42, 3989
Costa, A. 2005, GeoRL, 32, L22308
Demory, B.-O., Gillon, M., Deming, D., et al. 2011, A&A, 533, A114
Dingwell, D. B., Courtial, P., Giordano, D., & Nichols, A. R. L. 2004, E&PSL, 226, 127
Dumusque, X., Bonomo, A. S., Haywood, R. D., et al. 2014, ApJ, 789, 154
Elkins-Tanton, L. T. 2012, AREPS, 40, 113
Emile-Geay, J., & Madec, G. 2009, OcSci, 5, 203
Fiquet, G., Auzende, A. L., Siebert, J., et al. 2010, Sci, 329, 1516
Fofonoff, N. 1962, The Sea, 1, 3
Gelman, S. E., Elkins-Tanton, L. T., & Seager, S. 2011, ApJ, 735, 72
Ghosh, D. B., & Karki, B. B. 2011, GeCoA, 75, 4591
Ghosh, D. B., & Karki, B. B. 2016, NatSR, 6, 37269
Gibert, B., Seipold, U., Tommasi, A., & Mainprice, D. 2003, JGRB, 108
Hamano, K., Kawahara, H., Abe, Y., Onishi, M., & Hashimoto, G. L. 2015, ApJ, 806, 216
Haynes, W. M. 2014, CRC Handbook of Chemistry and Physics (Boca Raton, FL: CRC Press)
Heisel, M., de Silva, C. M., Hutchins, N., Marusic, I., & Guala, M. 2020, JFM, 887, R1
Herzberg, C., & Zhang, J. 1996, JGR, 101, 8271
Ingersoll, A. P., Summers, M. E., & Schlipf, S. G. 1985, Icar, 64, 375
Jiang, W., Wu, L., & Liu, Q. 2021, FrEaS, 9, 396
Kang, W., Ding, F., Wordsworth, R., & Seager, S. 2021, ApJ, 906, 67
Katsura, T., Yoneda, A., Yamazaki, D., Yoshino, T., & Ito, E. 2010, PEPI, 183, 212
Kite, E. S., Fegley, B., Jr, Schaefer, L., & Gaidos, E. 2016, ApJ, 828, 80
Léger, A., Grasset, O., Fegley, B., et al. 2011, Icar, 213, 1
Léger, A., Rouan, D., Schneider, J., et al. 2009, A&A, 506, 287
Lejeune, A.-M., & Richet, P. 1995, JGR, 100, 4215
Li, Q., Sun, L., & Xu, C. 2017, Open Journal of Marine Science, 8, 152
Liebske, C., Schmickler, B., Terasaki, H., et al. 2005, E&PSL, 240, 589
Luo, C., Gao, G., Xu, M., Yin, B., & Lv, X. 2023, Journal of Marine Science and Engineering, 11, 1487
Malavolta, L., Mayo, A. W., Louden, T., et al. 2018, AJ, 155, 107
Marshall, J., Adcroft, A., Hill, C., Perelman, L., & Heisey, C. 1997a, JGR, 102, 5753
Marshall, J., Hill, C., Perelman, L., & Adcroft, A. 1997b, JGR, 102, 5733
McDougall, T. J., & Feistel, R. 2003, DSRI, Papers, 50, 1523
Meier, T. G., Bower, D. J., Lichtenberg, T., Hammond, M., & Tackley, P. J. 2023, A&A, 678, A29
Mesinger, F., & Arakawa, A. 1976, Numerical Methods Used in Atmospheric Model, Vol. 1 (Global Atmospheric Research Programme)
Monteux, J., Andrault, D., & Samuel, H. 2016, E&PSL, 448, 140
Munk, W., & Wunsch, C. 1998, DSRI, 45, 1977
Nguyen, T. G., Cowan, N. B., Banerjee, A., & Moores, J. E. 2020, MNRAS, 499, 4605
Ni, H., Hui, H., & Steinle-Neumann, G. 2015, RvGeo, 53, 715
Nikolaou, A., Katyal, N., Tosi, N., et al. 2019, ApJ, 875, 11
Prandtl, L. 1925, ZAMM, 5, 136
Rintoul, M. D., & Torquato, S. 1996, JChPh, 105, 9258
Risien, C. M., & Chelton, D. B. 2008, JPO, 38, 2379
Sakamaki, T., Ohtani, E., Urakawa, S., Suzuki, A., & Katayama, Y. 2010, AmMin, 95, 144
Schaefer, L., & Fegley, B. 2009, ApJ, 703, L113
Scott, J. R., Marotzke, J., & Adcroft, A. 2001, JGR, 106, 31141
Sentchev, A., Yaremchuk, M., Bourras, D., Pairaud, I., & Fraunie, P. 2023, JAtOT, 40, 1291
Showman, A. P., Cho, J. Y.-K., & Menou, K. 2010, Atmospheric Circulation of Exoplanets, in Exoplanets, ed. S. Seager, 526 (Tucson, AZ: Univ. Arizona Press), 471
Solomatov, V. 2007, Magma Oceans and Primordial Mantle Differentiation, Treatise on Geophysics (Amsterdam: Elsevier), 91
Sterl, A. 2017, Roy. Netherland Met. Office. Tech. Rep, 361, 23
Stevenson, D. J. 2010, SSRv, 152, 651
Sun, Y., Zhou, H., Liu, X., Yin, K., & Lu, X. 2020, E&PSL, 551, 116556
Tokano, T., & Lorenz, R. D. 2016, Icar, 270, 67
Tosi, N., Plesa, A.-C., & Breuer, D. 2013, JGRE, 118, 1512
Valencia, D., Ikoma, M., Guillot, T., & Nettelmann, N. 2010, A&A, 516, A20
Vallis, G. K. 2019, Essentials of Atmospheric and Oceanic Dynamics (Cambridge: Cambridge Univ. Press)
Von Braun, K., Tabetha, S. B., Ten Brummelaar, T. A., et al. 2011, ApJ, 740, 49
Von Karman, T. 1930, Proc. of the Third International Congress of Applied Mechanics, 1930, 85
Wang, F., Huang, S.-D., Zhou, S.-Q., & Xia, K.-Q. 2016, JGRC, 121, 7589
Waterhouse, A. F., MacKinnon, J. A., Nash, J. D., et al. 2014, JPO, 44, 1854
Wunsch, C., & Ferrari, R. 2004, AnRFM, 36, 281
Zhang, Y. 2010, RvMG, 72, 5
Zhang, Y., Zhang, N., & Tian, M. 2022, AcGch, 41, 568
Zilinskas, M., Van Buchem, C., Miguel, Y., et al. 2022, A&A, 661, A126

The Planetary Science Journal, 5:205 (13pp), 2024 September https://doi.org/10.3847/PSJ/ad70b4

Ocean Circulation on Tide-locked Lava Worlds. II. Scalings

Yanhong Lai[1,2], Wanying Kang[3], and Jun Yang[1,2]

[1] Laboratory for Climate and Ocean-Atmosphere Studies, Department of Atmospheric and Oceanic Sciences, School of Physics, Peking University, Beijing 100871, People's Republic of China

[2] Institute of Ocean Research, Peking University, Beijing 100871, People's Republic of China

[3] Department of Earth, Atmosphere and Planetary Science, MIT, Cambridge, MA 02139, USA; wanying@mit.edu

Received 2024 February 16; revised 2024 August 14; accepted 2024 August 15; published 2024 September 24

Abstract

On tidally locked lava planets, a magma ocean can form on the permanent dayside. The circulation of the magma ocean can be driven by stellar radiation and atmospheric winds. The strength of ocean circulation and the depth of the magma ocean depend on external forcings and the dominant balance of the momentum equation. In this study, we develop scaling laws for the magma ocean depth, oceanic current speed, and ocean heat transport convergence driven by stellar and wind forcings in three different dynamic regimes: nonrotating viscosity-dominant Regime I, nonrotating inviscid limit Regime II, and rotation-dominant Regime III. Scaling laws suggest that magma ocean depth, current speed, and ocean heat transport convergence are controlled by various parameters, including vertical diffusivity/viscosity, substellar temperature, planetary rotation rate, and wind stress. In general, scaling laws predict that magma ocean depth ranges from a few meters to a few hundred meters. For Regime I, results from scaling laws are further confirmed by numerical simulations. Considering the parameters of a typical lava super-Earth, we found that the magma ocean is most likely in the rotation-dominant Regime III.

Unified Astronomy Thesaurus concepts: Exoplanet dynamics (490); Exoplanets (498); Habitable planets (695)

1. Introduction

On tidally locked lava planets, a magma ocean can form on the permanent dayside (A. Léger et al. 2009, 2011; N. M. Batalha et al. 2011; B.-O. Demory et al. 2011; X. Dumusque et al. 2014; E. S. Kite et al. 2016; V. Bourrier et al. 2018; L. Malavolta et al. 2018; T. G. Nguyen et al. 2020; K.-H. Chao et al. 2021; C. L. Brinkman et al. 2023). Given the high surface temperatures and the relatively advanced ages of lava worlds (A. Léger et al. 2009; N. M. Batalha et al. 2011), there is a possibility that volatile elements, such as C, N, and H, may have dissipated from these planets (D. Valencia et al. 2010). The atmospheric pressure, determined by the vaporization of underlying silicate melts (A. Léger et al. 2009; L. Schaefer & B. Fegley 2009; E. S. Kite et al. 2016), may exhibit significant gradients due to the diminishing stellar flux away from the substellar point (A. Léger et al. 2011; T. G. Nguyen et al. 2020). Thus, there are strong horizontal winds flowing outward from the substellar point (∼2000 m s^{-1}; T. Castan & K. Menou 2011; T. G. Nguyen et al. 2020; W. Kang et al. 2021).

Much remains unclear regarding the ocean on tidally locked lava planets. In most previous studies, the magma ocean depth is assumed to be determined by the adiabatic temperature profile (A. Léger et al. 2011; C.-É. Boukare et al. 2022). This assumption holds particularly true in scenarios within which a potent internal heat source dominates over stellar radiation (C.-É. Boukare et al. 2022). The prevalence of strong internal heating can sustain vigorous vertical convection, leading to an isentropic vertical temperature profile for which temperature increases with pressure following the adiabatic lapse rate (V. Solomatov 2007; Y. Zhang et al. 2022). Consequently, the magma ocean depth can extend to tens or even hundreds of kilometers (A. Léger et al. 2011; C.-É. Boukare et al. 2022).

Even in the presence of internal heating, vigorous convection may not occur within the magma ocean, unless (1) the resultant temperature increase with depth is greater than the increase of the liquidus with pressure, or (2) the resultant temperature increase leads to a supercritical Rayleigh number (a dimensionless number that describes the relationship between buoyancy and dissipative forces; V. Solomatov 2007) even in the solid phase. In the former situation, a second liquid layer would form in the interior, subject to convection, and in the latter situation, the solid mantle will convect. T. G. Meier et al. (2023) utilized 2D mantle convection models to investigate the magma ocean depth of 55 Cnc e under varying internal heating rates. Their findings suggest that the depth of the magma ocean could still reach approximately 500 km on the dayside, even without internal heating. However, it is important to note that their study did not account for the impact of ocean circulation and the resultant stratification on magma ocean depth.

The magma ocean depth will be controlled by ocean circulation when the internal heat source is weak or absent. This circumstance is plausible for tidally locked lava planets, particularly those that have undergone cooling over billions of years (such as CoRot-7b, Kepler-10b, and 55 Cnc e; N. M. Batalha et al. 2011; A. Léger et al. 2011; K. Von Braun et al. 2011; L. Malavolta et al. 2018; C. L. Brinkman et al. 2023). Ocean circulation is conceivable on lava planets, considering that the viscosity of fully molten silicates is comparable to that of seawater on Earth (D. B. Dingwell et al. 2004; W. M. Haynes 2014; Y. Sun et al. 2020; Y. Zhang et al. 2022). With a substantial surface temperature gradient and robust atmospheric winds (T. Castan & K. Menou 2011; A. Léger et al. 2011; W. Kang et al. 2021), both thermal and wind forcings can play crucial roles in driving the ocean circulation on lava planets.

The planetary parameters of lava planets and the oceanic parameters of magma oceans could vary significantly, implying

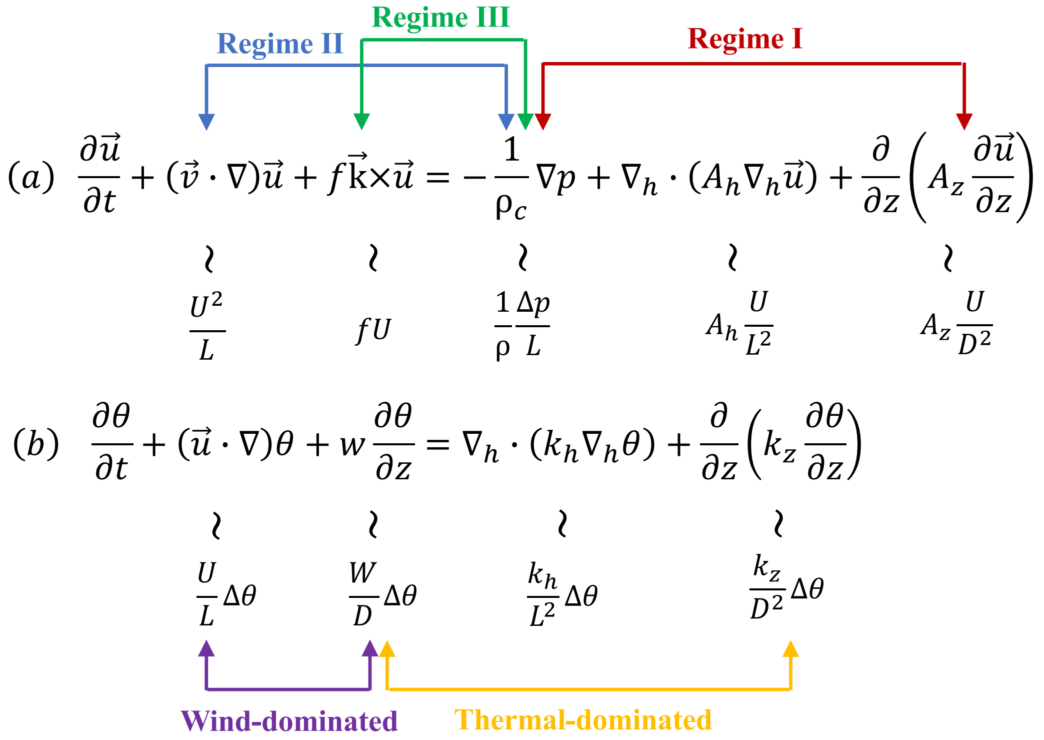

Figure 1. The general equations for horizontal momentum (a) and potential temperature (b) in the interior ocean, where $\boldsymbol{v} = u\boldsymbol{i} + v\boldsymbol{j} + w\boldsymbol{k}$; u, v, and w are the zonal, meridional, and vertical velocities, respectively; $\boldsymbol{u} = u\boldsymbol{i} + v\boldsymbol{j}$ is the horizontal velocity; f is the Coriolis parameter; ρ_c is the reference density; p is pressure; A_h and A_z are the horizontal and vertical viscosity coefficients, respectively; θ is the potential temperature; and k_h and k_z are the horizontal and vertical diffusivities, respectively. The characteristic scales of each term are presented below the equations. The dominant terms of the momentum equation in Regimes I, II, and III are shown in red, blue, and green brackets, respectively. The dominant terms of the thermal equation in thermal-dominated and wind-dominated systems are shown in gold and purple brackets, respectively.

that magma oceans on these lava planets can exist in different dynamic regimes. Tidally locked lava planets, such as Kepler-10b, CoRot-7b, 55 Cnc e, and K2-141b, typically have relatively fast rotation periods, around 1 Earth day (N. M. Batalha et al. 2011; A. Léger et al. 2011; V. Bourrier et al. 2018; L. Malavolta et al. 2018; C. L. Brinkman et al. 2023). A magma ocean may also form on slowly rotating terrestrial planets due to giant impacts (L. T. Elkins-Tanton 2012; K.-H. Chao et al. 2021).

This paper is Part II of a series of papers. In Part I, we investigated the ocean circulation on tidally locked lava planets using an idealized 2D numerical model developed by the authors (Ocean Circulation on Tide-locked Lava Worlds. Part I. An Idealized 2D Numerical Model). We presented the simulation results under thermal forcing only and under both thermal and wind forcings. We further compared our simulation results with previous studies. In general, simulation results under a weak or nonexistent internal heat source suggest an ocean depth on the order of 100 m, which is over 100 times shallower than that without ocean circulation. However, the Coriolis force is neglected in Part I, which could play a significant role in ocean circulation (E. S. Kite et al. 2016; G. K. Vallis 2019).

Here, we present scaling laws for magma ocean depth, oceanic current speed, and ocean heat transport convergence in three dynamical regimes (Figure 1): nonrotating viscosity-dominant Regime I in Section 2.1, nonrotating inviscid limit Regime II in Section 2.2, and rotation-dominant Regime III in Section 2.3. We present the comparison between the results from scaling laws and numerical simulations in Regime I in Section 2.1. We discuss the parameter space within which each of the scaling laws is applicable in Section 3. In Section 4, conclusions are presented.

2. Scaling Laws for Magma Ocean Depth, Current Speed, and Ocean Heat Transport Convergence

There are three major driving forces in the system: (1) thermal forcing from the star, (2) wind stress induced by the day-to-nightside atmospheric flow, and (3) surface evaporation and condensation. Our work here focuses on the first two types of forcing. The third one is left for future study.

On lava worlds, the stellar radiative flux is in the order of $10^6\ \mathrm{W\,m^{-2}}$, which has been shown to be 2–3 orders of magnitude greater than the heat rates induced by other physical processes, such as advection (E. S. Kite et al. 2016; W. Kang et al. 2021). The dominance of stellar radiative flux justifies our setting the surface temperature to the radiative equilibrium temperature. The wind stress, i.e., the momentum exchange between the atmosphere and ocean, is induced by the deposition of atmospheric mass with nonzero velocity and momentum transport by turbulent eddies (A. P. Ingersoll et al. 1985). On tidally locked lava planets, eddy transport dominates given that the wind speed V_a can reach $\sim 2000\ \mathrm{m\,s^{-1}}$ (T. Castan & K. Menou 2011; T. G. Nguyen et al. 2020; W. Kang et al. 2021). Only accounting for this component, the wind stress on such planets can be estimated as $\tau = \rho_a C_D V_a^2$, where $\rho_a \sim 10^{-2}\ \mathrm{kg\,m^{-3}}$ represents atmospheric density (W. Kang et al. 2021) and C_D represents the surface drag coefficient. Assuming $C_D \sim 10^{-2}$ under high wind speeds (A. Sterl 2017; W. Jiang et al. 2021), the wind stress is approximately

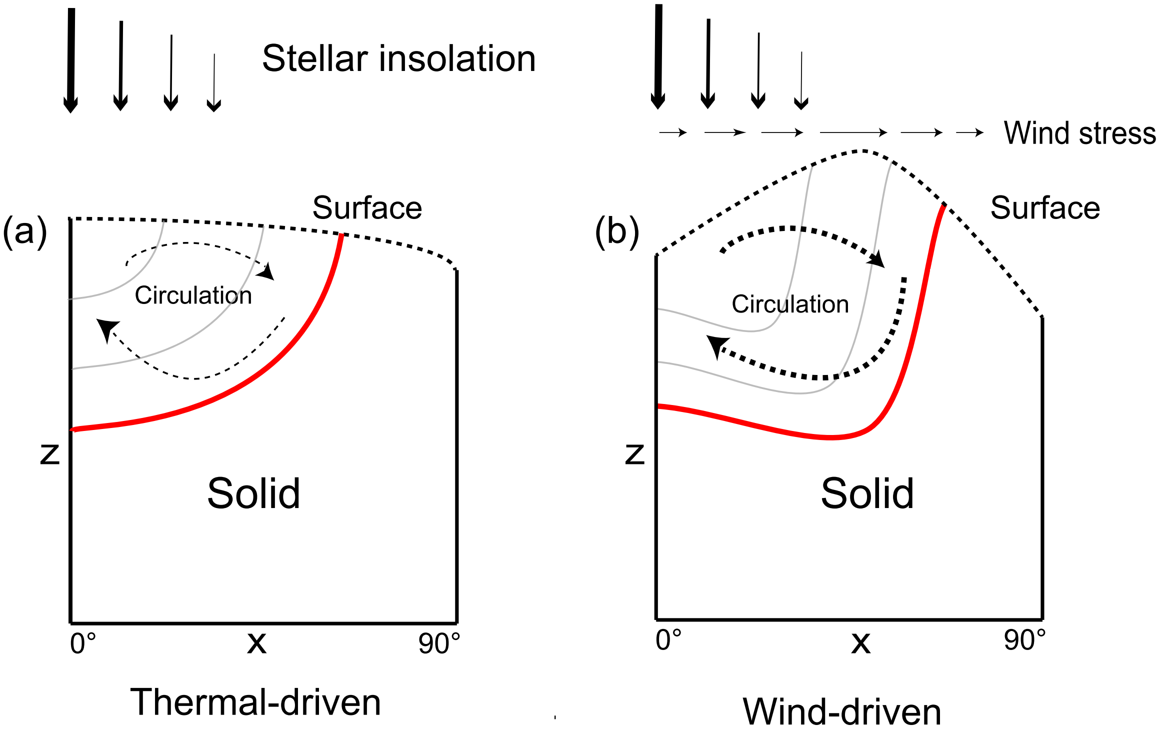

Figure 2. Schematics of thermal-driven (a) and wind-driven (b) ocean circulations. In the schematics, the external forcings, surface height, ocean circulation, and magma ocean depth are shown. The red solid line represents the boundary of the magma ocean, and the gray lines represent the isotherms, indicating that temperature decreases as depth increases within the ocean. For more details, please see Part I.

100 N m^{-2}. More details of the wind stress calculation can be found in Part I of this series of papers.

When the stellar radiative forcing dominates (see Figure 2(a)), the magma ocean circulation is mainly powered by the density gradient induced by the attenuation of stellar flux away from the substellar point. Under this forcing, the fluid density increases with x, the distance away from the substellar point, driving an ocean current toward the substellar point in the lower part of the ocean. In an equilibrium state, net transport across a different depth z needs to vanish, so the surface fluid needs to flow toward the edge of the magma ocean, facilitated by the pressure gradient induced by the sea surface elevation anomaly.

When the wind stress dominates (see Figure 2(b)), the surface fluid will be pushed toward the magma ocean edge, creating a high sea surface height there. This high sea surface height then forces fluid back toward the substellar point in the lower levels. Although the circulation in both the thermal- and wind-driven systems features sinking motions along the magma ocean edge and upwelling motions near the substellar point, the shape of the sea surface and the liquid–rock boundary differs.

In the presence of ocean circulation, the ocean temperature profile differs from that without such circulation (A. Léger et al. 2011; C.-É. Boukare et al. 2022). Since both forcings cause cold magma formed at the magma ocean edge to sink, filling the bottom ocean, the temperature in the ocean should decrease with depth from the surface temperature to the liquidus (Figure 2). Below the ocean bottom, vertical diffusion governs the temperature profile, which should be uniform at a temperature just below the liquidus. For more details, please see Part I of our work. Here, we focus on the magma ocean depth determined by the ocean circulation.

As will be shown later, vertical diffusivity and viscosity play a key role in determining the magma ocean circulation strength and depth by controlling the rate at which dense fluid can be pumped back up to the surface and the rate momentum can be transported vertically. Diffusivity and viscosity of molten silicates are contributed by both molecular random motions and turbulent fluid motions. While molecular diffusivity varies from 10^{-9} to 10^{-8} m^2 s^{-1} at a temperature of 2000–3000 K (D. B. Ghosh & B. B. Karki 2011) and molecular viscosity is around 10^{-4} m^2 s^{-1} (Y. Sun et al. 2020; Y. Zhang et al. 2022), turbulence-induced diffusivity/viscosity powered by winds and tides remains largely unconstrained. In Earth's oceans, vertical mixing is mainly contributed by turbulence, yielding a vertical diffusivity of around 10^{-5}–10^{-3} m^2 s^{-1} (W. Munk & C. Wunsch 1998; A. F. Waterhouse et al. 2014) and a vertical viscosity of around 10^{-3}–10^{-1} m^2 s^{-1} (C. Luo et al. 2023; A. Sentchev et al. 2023), several orders of magnitude greater than the molecular diffusivity/viscosity. Given the large uncertainty, we explore a wide range of diffusivity and viscosity values, ranging from 10^{-7} to 10^{-3} m^2 s^{-1} and 10^{-7} to 10^2 m^2 s^{-1}, respectively.

In this section, we present scaling laws for the horizontal velocity, magma ocean depth, and ocean heat transport convergence in three dynamical regimes that feature different dominant balances in the momentum equation: nonrotating viscosity-dominant Regime I (Section 2.1), nonrotating inviscid limit Regime II (Section 2.2), and rotation-dominant Regime III (Section 2.3). In Regimes I, II, and III, the pressure gradient force is balanced by the vertical viscosity, nonlinear advection, and Coriolis force in the momentum equation, respectively. Figure 1(a) shows the general horizontal momentum equation and marks the dominant terms in each dynamical regime. Note that geometry introduces additional metric terms into the equations. However, from a scaling perspective, these metric terms do not affect the final results up to a constant factor. Also, it has been shown that the influence of varying coordinates on the dynamics of tidally locked planets might be limited (M. Hammond & R. T. Pierrehumbert 2018; S. Wang & J. Yang 2021; J. Yang et al. 2023).

For each dynamic regime, the predominant terms in the thermal equation vary depending on whether ocean circulation is predominantly driven by thermal or wind forcings (G. K. Vallis 2019). When wind forcing is absent or weak, vertical advection and vertical diffusion take precedence over other terms in the thermal equation (gold bracket in Figure 1(b)). Conversely, when wind forcing is significant, horizontal advection and vertical advection become dominant (purple bracket in Figure 1(b)). Thus, we provide two scaling laws in each dynamic regime, which describe the magma ocean depth D, horizontal velocity U, and ocean heat transport convergence H dominated by thermal and wind forcings, respectively. Knowing the strengths of the two forcings, one could evaluate D, U, and H following the two scaling laws and choose whichever gives the larger value for D, U, and H. This will guarantee that the scaling law for the dominant type of forcing gets selected.

2.1. Regime I: Nonrotating Viscosity-dominant Regime

In the nonrotating regime, the Coriolis force is neglected, which guarantees the azimuthal symmetry of the circulation; i.e., the dynamics only varies with depth z and distance from the substellar point x. Further, if the vertical viscosity coefficient is large, the momentum budget will be in balance between the pressure gradient force and vertical viscosity (red brackets in Figure 1(a)).

The dominant balance of momentum equation gives

$$\frac{1}{\rho_c}\frac{\partial p}{\partial x} \approx \frac{\partial}{\partial z}\left(A_z \frac{\partial u}{\partial z}\right), \tag{1}$$

where u is the horizontal velocity, ρ_c is the reference density, A_z is the vertical viscosity coefficient, and $p = \rho_c g\eta - \rho_c \int_z^0 b dz$ is the pressure, where $b = -g\frac{\rho}{\rho_c}$ is buoyancy, g is gravity, ρ is density, and η is the sea surface height. Near the surface, the pressure gradient is dominated by the sea surface height variation, driving a flow away from the substellar point, whereas the pressure gradient near the bottom of the ocean should be dominated by the integrated buoyancy anomaly, driving a return flow toward the substellar point. For the pressure gradient to reverse in the vertical direction, the integrated buoyancy anomaly should be of the same magnitude as the pressure gradient. It should be noted that, in our study, the magma ocean boundary is set by the liquidus, where the magma viscosity is generally low, so that the vertical viscosity A_z may be considered as a constant throughout our domain.

In the interior ocean, mass continuity is always satisfied,

$$\frac{\partial u}{\partial x} + \frac{\partial w}{\partial z} = 0, \tag{2}$$

where w denotes the vertical velocity. When wind forcing is weak, the dominant driver of the circulation is diffusion. Along the magma ocean edge, fluid cools and sinks to the bottom, releasing gravity potential energy. In a stably stratified ocean, vertical mixing induced by tidal and wind-driven wave breaking can pump denser fluid upward, thereby increasing the gravitational potential energy of the system (C. Wunsch & R. Ferrari 2004). In the upwelling regions near the substellar point, the downward diffusive heat/buoyancy flux needs to balance the upward advective heat/buoyancy flux, leading to the so-called advective–diffusive balance (the gold bracket in Figure 1(b)),

$$w\frac{\partial \theta}{\partial z} = \kappa_z \frac{\partial^2 \theta}{\partial z^2}, \tag{3}$$

where θ denotes potential temperature and k_z denotes vertical diffusivity.

Thus, the scales of Equations (1), (2), and (3) could be written as

$$\frac{\Delta b}{L} D \sim A_z \frac{U}{D^2}, \tag{4}$$

$$\frac{U}{L} \sim \frac{W}{D}, \tag{5}$$

$$D \sim \frac{k_z}{W}, \tag{6}$$

where U, W, L, D, and Δb represent the typical scales of horizontal velocity, vertical velocity, horizontal range of the magma ocean, magma ocean depth, and horizontal buoyancy difference, respectively. Especially, $\Delta b \sim g\alpha\Delta T$ utilizing the linear equation-of-state approximation, where α is the thermal expansion coefficient and ΔT is the horizontal potential temperature difference within the ocean. Note that the mass continuity equation (Equation (2)) is written in a Cartesian coordinate. If it is rewritten for a disk coordinate, the first term of Equation (2) will change to $\frac{1}{x}(\frac{\partial ux}{\partial x})$, but this change will not affect the scaling presented in Equation (5).

Combining these three constraints, we are able to determine the characteristic scales for the magma ocean depth D_{1t} as well as the horizontal current speed U_{1t},

$$D_{1t} \sim \left(\frac{k_z A_z L^2}{\Delta b}\right)^{1/5},\ U_{1t} \sim \left(\frac{\Delta b^2 k_z^3 L}{A_z^2}\right)^{1/5}. \tag{7}$$

Ocean circulation redistributes heat within the magma ocean basin. The resultant heating rate can drive the surface temperature away from radiative equilibrium. Following R. Ferrari & D. Ferreira (2011), we estimate the ocean heat convergence (H),

$$H = \frac{\partial}{\partial x}\int_{-D}^{0} \rho c_p u\theta dz \sim \rho c_p \Delta T \frac{UD}{L}, \tag{8}$$

where c_p represents the heat capacity at constant pressure. By substituting the scaling laws of the current speed U_{1t} and ocean depth D_{1t} (Equation (7)) into Equation (8), we obtain the ocean heat convergence (H_{1t}),

$$H_{1t} = \frac{\rho c_p}{g\alpha}\left(\frac{k_z^4 \Delta b^4}{A_z L^2}\right)^{1/5}. \tag{9}$$

Under strong wind forcing, the main driving force of the ocean circulation shifts from thermal to wind forcing. Induced by winds and viscosity, there will be a boundary layer, in which wind forcing balances with vertical viscosity. Given the relatively large viscosity here, the boundary layer depth could be approximated to be comparable to the magma ocean depth.

Thus, the momentum equation gives

$$\frac{1}{\rho_c}\frac{\partial \tau}{\partial z} \approx \frac{\partial}{\partial z}\left(A_z \frac{\partial u}{\partial z}\right), \tag{10}$$

which scales as

$$\frac{\tau}{\rho} \sim A_z \frac{U}{D}, \tag{11}$$

where τ represents wind stress. The momentum balance between the pressure gradient force and vertical viscosity still works in the interior ocean (Equation (1)), despite the presence of wind stress. Thus, combining Equations (4) and (11), the characteristic scales for the magma ocean depth D_{1w} and horizontal velocity U_{1w} under strong wind forcing are expressed as

$$D_{1w} \sim \left(\frac{\tau L}{\rho \Delta b}\right)^{1/2},\ U_{1w} \sim \left(\frac{\tau^3 L}{\rho^3 A_z^2 \Delta b}\right)^{1/2}. \tag{12}$$

Substituting Equation (12) into Equation (8), we obtain the ocean heat transport convergence under wind forcing (H_{1w}),

$$H_{1w} \sim \frac{c_p}{g\alpha}\frac{\tau^2}{\rho A_z}. \tag{13}$$

To estimate and compare the magma ocean depth, horizontal current speed, and ocean heat transport convergence under varying parameters and forcings, we adopt the planetary parameters of Kepler-10b, including the planet radius (a), gravity (g), and substellar temperature (T_{sub}) (X. Dumusque et al. 2014). The baseline values of the planetary and oceanic parameters used in Figures 3–6 are summarized in Table 1. By default, planetary rotation and wind stress are not included. Notably, the temperature contrast within the magma ocean (ΔT) is determined by the difference between the substellar temperature and the liquidus, while the horizontal scale of the magma ocean (L) is governed by the substellar temperature, the liquidus, and the planet radius.

We start by discussing and validating the scaling results in a thermal-dominated system. When the main driving factor of the circulation is thermal forcing, scaling laws indicate that magma ocean depth, horizontal velocity, and ocean heat transport convergence are determined by vertical diffusivity, surface temperature/buoyancy difference, and vertical viscosity (Equations (7) and (9)). As vertical viscosity/diffusivity increases, the influence of the surface forcings can reach deeper depths, increasing the magma ocean depth D. Then the variation of horizontal velocity differs when the vertical viscosity and diffusivity change. A higher vertical diffusivity deepens the magma ocean depth, which then requests a faster flow speed to balance the same level of pressure gradient force (Equation (4)). In contrast, a higher vertical viscosity results in a weaker vertical upwelling speed W as the diffusion pump needs to pump fluid from deeper depths (Equation (6)). This in turn leads to a weaker horizontal flow U under the constraint of mass continuity (Equation (5)). Due to the relatively limited change of ocean depth, the variation of heat transport convergence is dominated by the variation of horizontal velocity (Equation (9)). Thus, heat transport convergence H increases as vertical diffusivity increases and vertical viscosity decreases.

The scaling predictions for varying vertical viscosities are presented in Figures 3(a), (c), and (e) and 4(a), (e), and (h). In order for the solutions to fall in the viscosity-dominant regime (Regime I), the vertical viscosity term needs to dominate the advection and Coriolis force terms (see Section 3 for a detailed discussion). This requires a relatively large vertical viscosity. Therefore, we only show scaling results for a vertical viscosity ranging from 10^{-3} to 10^{2} m^2 s^{-1}.

The dependence of the magma ocean depth, flow speed, and heat transport convergence on varying parameters predicted by scaling laws here is confirmed by numerical simulations (scattered points of Figures 3 and 4). The experiments presented here are taken from Part I of this series of papers. The model solves the zonal momentum, thermal, mass continuity, and sea surface height equations using the finite difference method under 2D (x–z) Cartesian geometry. At the surface, the system is forced by thermal or wind forcing. The thermal forcing is represented by strong relaxation toward the radiative equilibrium temperature. The wind forcing is represented by prescribing the momentum flux injected into the upper surface of the ocean. At the bottom layer, the vertical velocity is set to zero, and the zonal velocity is strongly damped to guarantee an almost zero velocity. A no-flux boundary condition is used for temperature there. Details of the integration scheme and parameter choice can be found in Part I.

As predicted, the simulated magma ocean depth D deepens as vertical viscosity A_z and vertical diffusivity k_z increase. When A_z increases from 10^0 to 10^2 m^2 s^{-1}, D deepens from about 400 to 920 m, accompanied by U decreased from 0.24 to 0.03 m s^{-1} (scattered points in Figures 3(a) and (c)). Meanwhile, heat transport convergence H decreases from 2.5×10^4 to 3.2×10^3 W m^{-2} (scattered points in Figure 3(e)). When k_z changes from 10^{-6} to 10^{-4} m^2 s^{-1}, D increases from 160 to 800 m, with U intensified from 0.008 to 0.09 m s^{-1}, causing H to increase from 5.8×10^2 to 7.8×10^3 W m^{-2} (scattered points in Figures 3(a), (c), and (e)). The results from numerical simulations well match that from scaling laws, as can be seen in Figures 4(a), (b), (e), (f), (h), and (i). Since the heat convergence H is 2–3 orders of magnitude smaller than the radiative flux, we do not expect the sea surface temperature to significantly deviate from the radiative equilibrium temperature, consistent with our assumptions.

The substellar temperatures of lava planets vary significantly (N. M. Batalha et al. 2011; T. Castan & K. Menou 2011; B.-O. Demory et al. 2011; A. Léger et al. 2011; T. G. Nguyen et al. 2020). Here, we change the substellar temperature from 2000 to 3500 K, and the corresponding scaling predictions are presented in Figures 3(b), (d), and (f) and 4(c), (g), and (j). Given that the liquidus is assumed to be 2000 K (J. Monteux et al. 2016), the correspondent temperature difference ranges from 0 to 1500 K. As the substellar temperature increases, two things happen simultaneously. First, the surface temperature difference will increase, and that will result in a stronger pressure gradient force. Consequently, both the horizontal and vertical velocities increase, which means the gravitational potential energy is consumed and the stratification is enhanced at a faster rate. Following the advective–diffusive balance, a fixed vertical diffusivity can only pump dense fluid up faster if the pumping depth is shallower (Equation (6)). Second, the width of the magma ocean also increases, and that will lead to a deeper magma ocean under the constraint of mass continuity (Equation (5)). The two effects cancel each other, making the

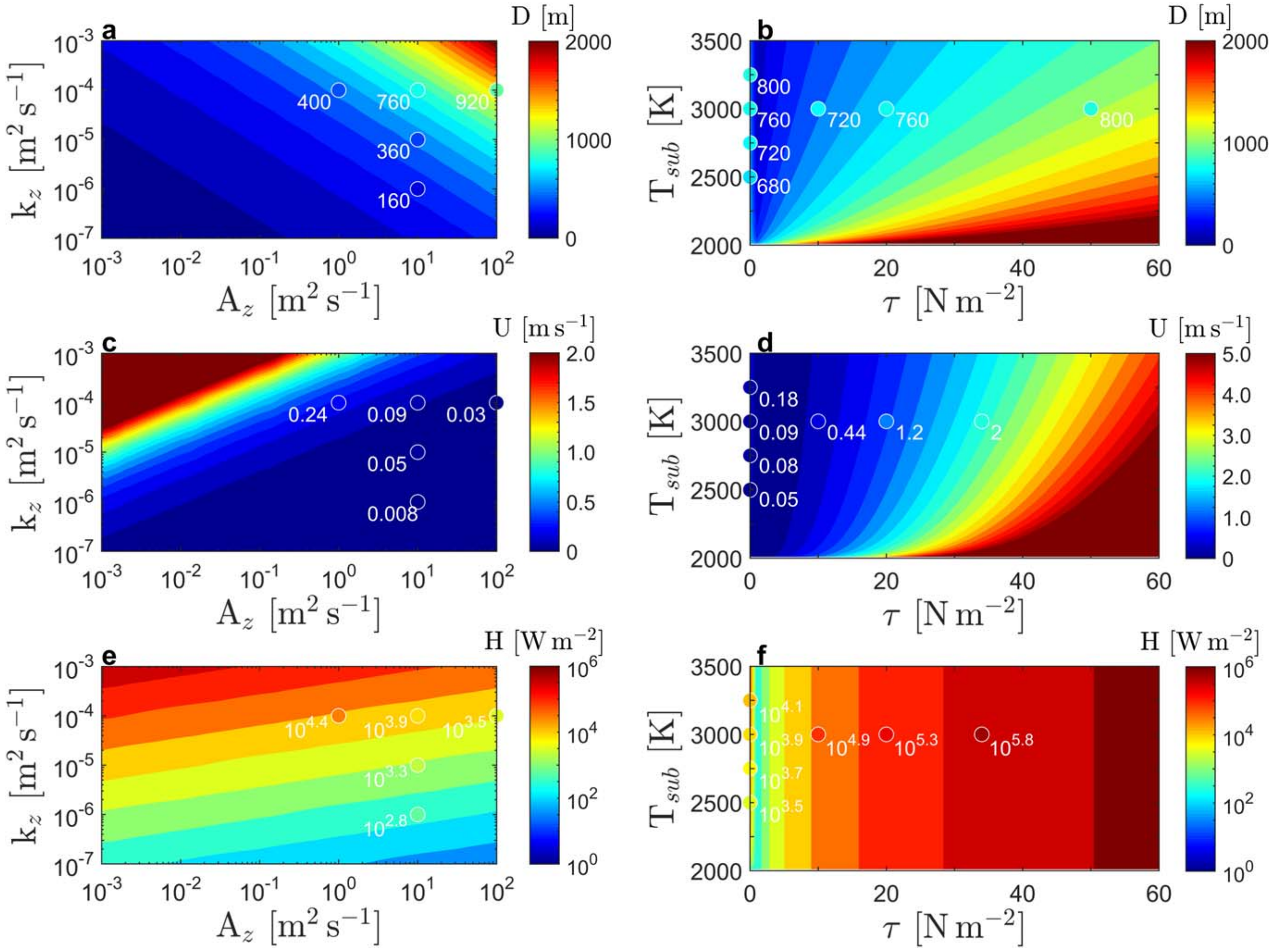

Figure 3. Scaling laws of the magma ocean depth (D; top), horizontal velocity (U; middle), and ocean heat transport convergence (H; bottom) in Regime I. Left panels: sensitivity of D, U, and H to vertical viscosity (A_z) and vertical diffusivity (k_z) when dominated by thermal forcing. Right panels: sensitivity of D, U, and H to wind stress (τ) and substellar temperature (T_{sub}) when dominated by wind forcing. Note that in the right panels, the results are still from the thermal-forcing-dominated scaling when the wind stress is zero. Colors are the results from scaling laws, and filled circles are the results from numerical simulations. For the numerical results, their exact values are indicated.

magma ocean depth insensitive to the change of substellar point temperature. The change of heat transport convergence is dominated by the variation of the current speed, which intensifies as the substellar temperature increases.

Numerical results under varying substellar temperatures T_{sub} show that as T_{sub} rises from 2500 to 3250 K, the magma ocean depth D increases from 680 to 800 m, with horizontal velocity U increased from 0.05 to 0.18 m s^{-1} (scattered points of Figures 3(b) and (d)). As a result, heat transport convergence increases from 3.3×10^3 to 1.2×10^4 W m^{-2} (scattered points of Figure 3(f)). Simulation results indicate that the dependence of magma ocean depth on substellar temperature is relatively weak, consistent with predictions from scaling laws. However, for unclear reasons, the two trends are opposite (Figure 4(c)).

We then discuss the scaling results in a wind-dominated system and verify the scaling using numerical experiments (Equations (12) and (13)). Here, scaling predictions are presented in Figures 3(b), (d), and (e) and 4(d), (h), and (k) for wind stress between 0 and 60 N m^{-2}. As the wind stress increases, scaling laws predict that the magma ocean depth, horizontal velocity, and heat transport convergence should increase. In particular, the wind forcing on Kepler-10b might reach a maximum value of 100 N m^{-2}, and it does dominate the thermal forcing as the major driver of the ocean circulation.

We conduct numerical simulations with wind stress τ set to 10, 20, and 34 N m^{-2}, and the results are shown by scattered points in Figures 3(b), (d), and (f). When τ increases from 10 to 34 N m^{-2}, magma ocean depth D increases from 720 to 800 m, accompanied by horizontal velocity U intensified from 0.44 to 2.0 m s^{-1}. The increase of both D and U results in the increase of H, which changes from 7.8×10^4 to 6.1×10^5 W m^{-2}. Results from scalings and simulations are consistent (Figures 4(d), (h), and (k)).

2.2. Regime II: Nonrotating Inviscid Limit Regime

The viscosity of fully molten silicates might be decreased to 10^{-4} or 10^{-5} m^2 s^{-1} (Y. Sun et al. 2020; Y. Zhang et al. 2022). Thus, the solutions in Regime I might not work when an extremely weak viscosity is considered. Here, we present scaling laws to the horizontal current speed, magma ocean depth, and ocean heat transport convergence under the nonrotating inviscid limit regime. Similar to Regime I, the Coriolis force is neglected. Under the inviscid limit, the pressure gradient force is balanced by the nonlinear advection in the momentum budget (blue brackets in Figure 1(a)). Then

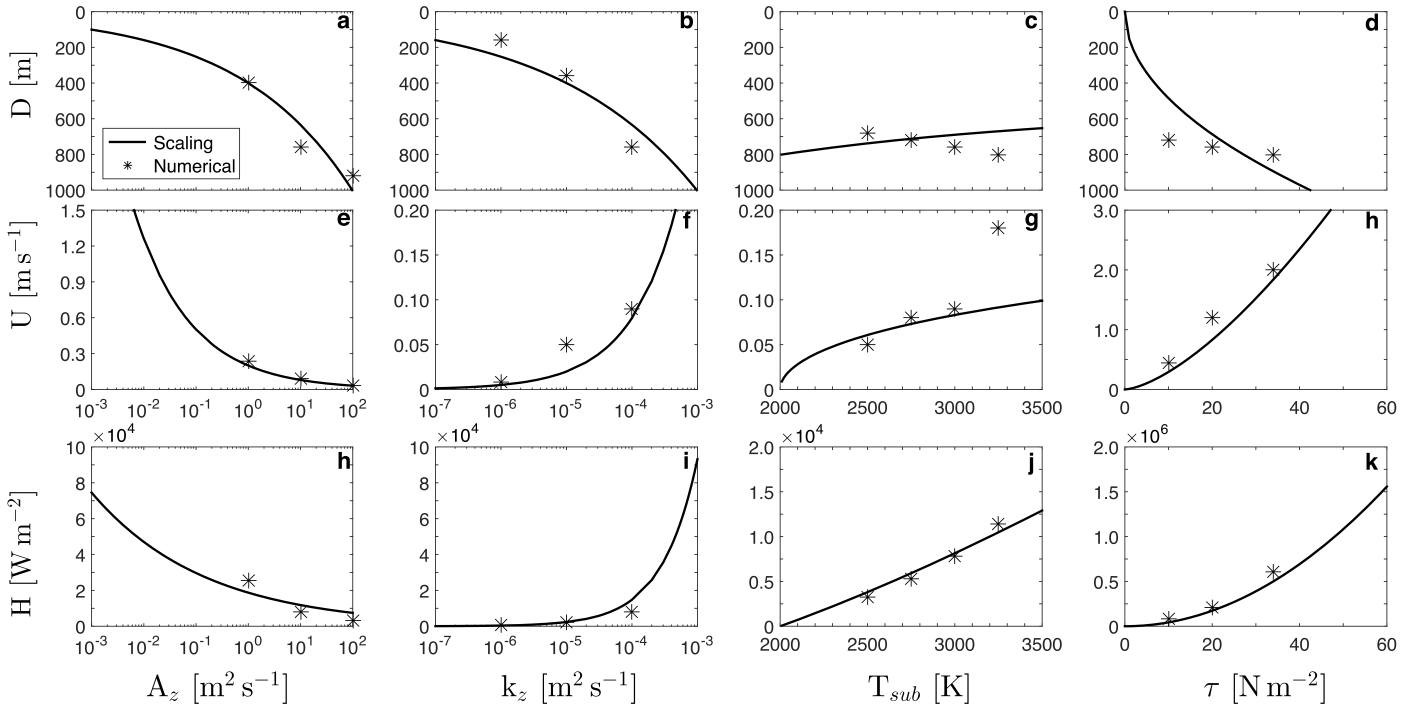

Figure 4. Comparison between results from scaling laws and from numerical simulations in Regime I. From left to right columns: sensitivity of the magma ocean depth D (top), horizontal velocity U (middle), and ocean heat transport convergence H (bottom) to vertical viscosity (A_z), vertical diffusivity (k_z), substellar temperature ($T_{\rm sub}$), and wind stress (τ). The solid lines and scattered asterisks are the results from scaling laws and numerical simulations, respectively. By default, wind forcing is not included, except for the rightmost series of results.

the dominant balance of the momentum equation is

$$\frac{1}{\rho_c}\frac{\partial p}{\partial x} \approx u\frac{\partial u}{\partial x}, \tag{14}$$

which scales as

$$\frac{\Delta b}{L}D \sim \frac{U^2}{L}. \tag{15}$$

Similar to that in Regime I, the mass continuity needs to be satisfied within the magma ocean, and the buoyancy is in balance between upwelling and diffusion. Employing Equations (5), (6), and (15), the magma ocean depth (D_{2t}) and horizontal current speed (U_{2t}) scale as

$$D_{2t} \sim \left(\frac{k_z^2 L^2}{\Delta b}\right)^{1/5},\ U_{2t} \sim (\Delta b^2 k_z L)^{1/5}. \tag{16}$$

Substituting Equation (16) into Equation (8), we obtain the ocean heat transport convergence (H_{2t}),

$$H_{2t} \sim \frac{\rho c_p}{g\alpha}\left(\frac{k_z^3 \Delta b^6}{L^2}\right)^{1/5}. \tag{17}$$

In the presence of wind forcing, the effect of wind forcing depends on the specific value of the vertical viscosity. If the viscosity of the magma surface is entirely zero, the magma ocean will not have any influence on the atmospheric momentum. In other words, the magma ocean will not be affected by the atmospheric winds. But if the viscosity is not exactly zero but a small number, wind stress can potentially influence the magma ocean. Here, we estimate the impacts assuming a small viscosity.

Given the smallness of the viscosity, only a very thin boundary layer near the surface will be directly influenced by wind stress. There, the dominant momentum balance is between the vertical viscosity and nonlinear advection, and the vertical viscosity scales with wind stress:

$$u\frac{\partial u}{\partial x} \approx \frac{\partial}{\partial z}\left(A_z\frac{\partial u}{\partial z}\right) \sim \frac{1}{\rho_c}\frac{\partial \tau}{\partial z}. \tag{18}$$

This leads to the following scale relationships:

$$\frac{U_v^2}{L} \sim A_z\frac{U_v}{D_v^2} \sim \frac{\tau}{\rho D_v}, \tag{19}$$

from which U_v and D_v are expressed as

$$U_v \sim \left(\frac{\tau^2 L}{\rho^2 A_z}\right)^{1/3},\ D_v \sim \left(\frac{\rho A_z^2 L}{\tau}\right)^{1/3}, \tag{20}$$

where U_v and D_v represent the typical scales of the horizontal velocity in the boundary layer and the depth of the boundary layer, respectively.

Then the interior vertical velocity W induced by the horizontal convergence/divergence of mass transport in the boundary layer should follow

$$W \sim \frac{U_v D_v}{L} \sim \left(\frac{\tau A_z}{\rho L}\right)^{1/3}. \tag{21}$$

Replacing Equation (6) and employing Equations (5), (15), and (21), the scales for the magma ocean depth (D_{2w}) and

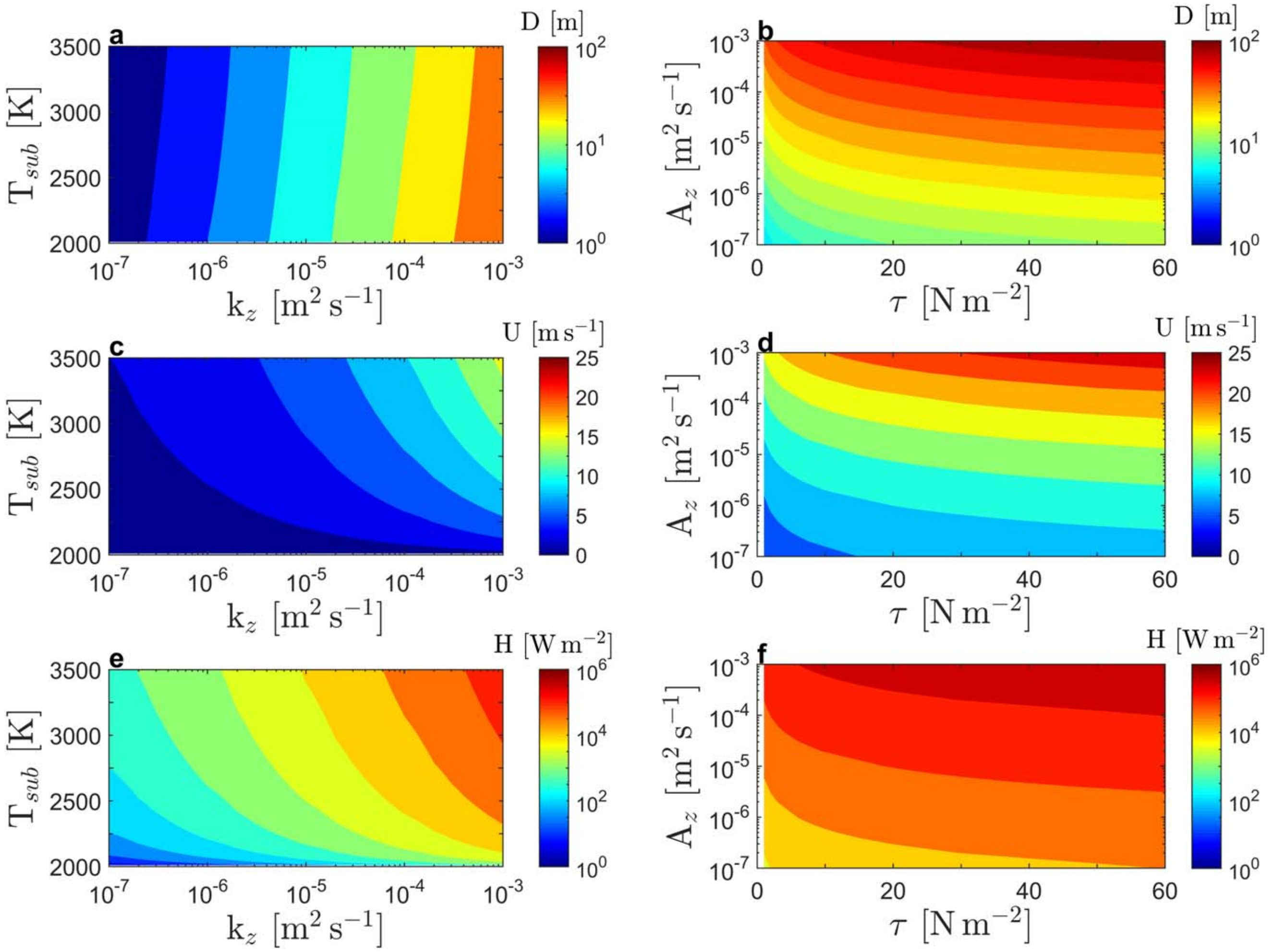

Figure 5. Scaling laws of the magma ocean depth (D; top), horizontal velocity (U; middle), and ocean heat transport convergence (H; bottom) in Regime II. Left panels: sensitivity of D, U, and H to vertical diffusivity (k_z) and substellar temperature ($T_{\rm sub}$) when dominated by thermal forcing. Right panels: sensitivity of D, U, and H to wind stress (τ) and vertical viscosity (A_z) when dominated by wind forcing.

horizontal velocity (U_{2w}) are

$$D_{2w} \sim \left(\frac{\tau^2 A_z^2 L^4}{\rho^2 \Delta b^3}\right)^{1/9},\; U_{2w} \sim \left(\frac{\Delta b^3 \tau A_z L^2}{\rho}\right)^{1/9}. \qquad (22)$$

Similarly, substituting Equation (22) into Equation (8), the scaling for ocean heat transport convergence (H_{2w}) is written as

$$H_{2w} \sim \frac{g}{g\alpha}\left(\rho^2 \Delta b^3 \frac{\tau A_z}{L}\right)^{1/3}. \qquad (23)$$

Results from the scaling laws in Regime II are presented in Figure 5. Due to the weak viscosity/diffusivity, the magma ocean depth will not exceed 100 m across the parameter range we consider here, much thinner than that in Regime I.

When dominated by thermal forcing, magma ocean depth, horizontal velocity, and heat transport convergence are mainly determined by vertical diffusivity and surface temperature difference (Equations (16) and (17)). Similar to Regime I, as vertical diffusivity increases, the magma ocean deepens following the advection–diffusion balance (Equation (6)), accompanied by increased horizontal velocity and heat transport convergence (Figures 5(a), (c), and (e)). Varying substellar temperatures lead to changes in the surface temperature difference, i.e., the pressure gradient force. Thus, the horizontal velocity increases under a larger temperature difference (higher substellar temperature), leading to stronger heat transport convergence. Meanwhile, the magma ocean becomes shallower due to stronger vertical velocity (Figures 5(a), (c), and (e)).

When dominated by wind forcing, magma ocean depth, horizontal velocity, and heat transport convergence are affected by the amplitude of wind stress and vertical viscosity (Equations (22) and (23)). Results with vertical viscosity ranging from 10^{-7} to 10^{-3} m^2 s^{-1} are shown in Figures 5(b), (d), and (f), in which the vertical viscosity discussed is much smaller than that in Regime I. As the vertical viscosity decreases, the wind-induced boundary layer is shallower, accompanied by weaker horizontal velocity in the boundary layer, which will then lead to weakening of the vertical velocity in the interior (Equations (20) and (21)). Magma ocean depth here, determined by the horizontal and vertical advections, becomes shallower. The interior horizontal velocity is determined by the balance between the pressure gradient force and nonlinear advection (Equation (15)). Thus, a shallower magma ocean corresponds to a smaller pressure gradient, decreasing the horizontal velocity. The decreases of both ocean depth and current speed result in the decrease of heat transport convergence (Equation (23)).

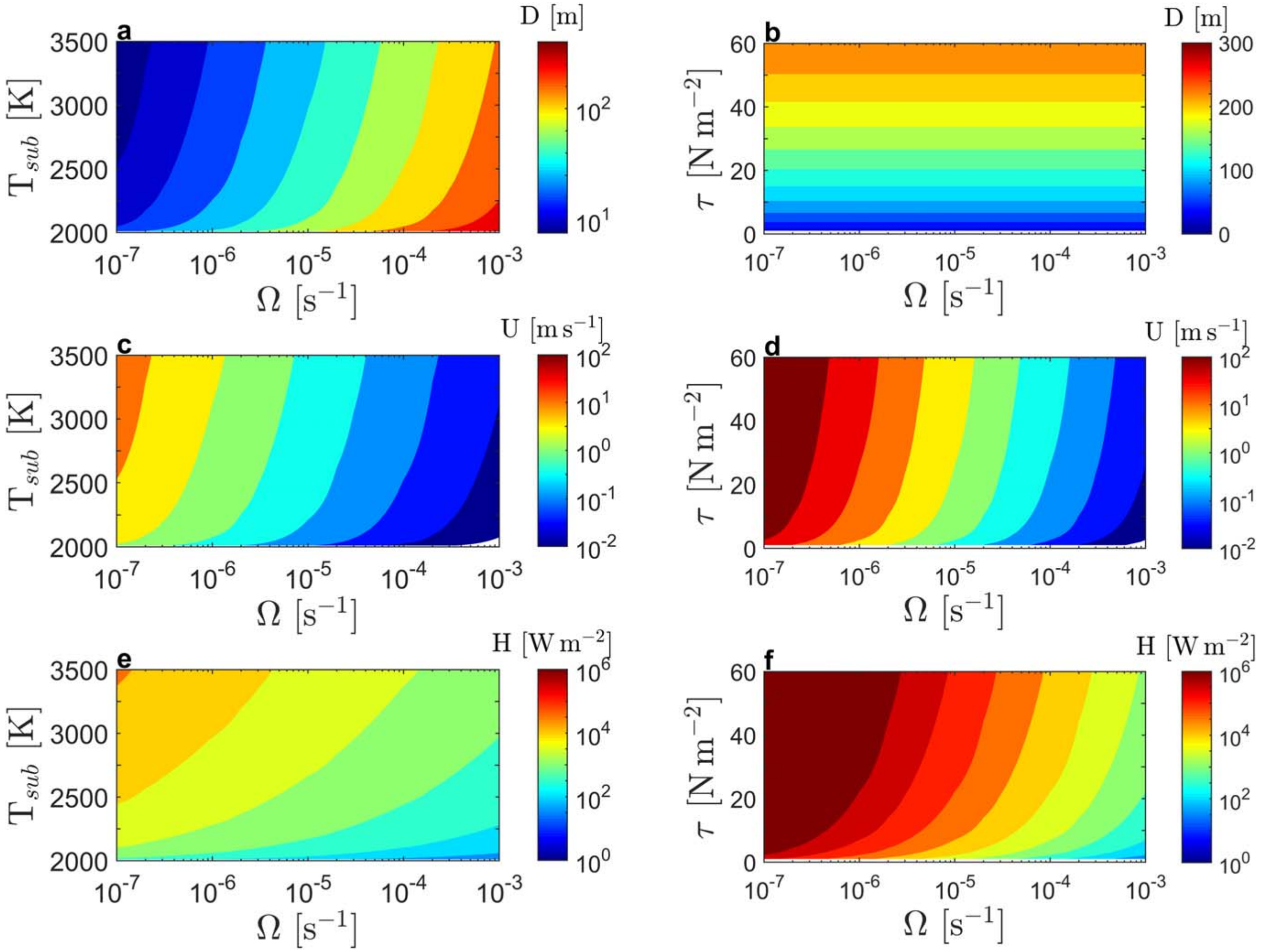

Figure 6. Scaling laws of the magma ocean depth (D; top), horizontal velocity (U; middle), and ocean heat transport convergence (H; bottom) in Regime III. Left panels: sensitivity of D, U, and H to planetary rotation rate (Ω) and substellar temperature ($T_{\rm sub}$) when dominated by thermal forcing. Right panels: sensitivity of D, U, and H to planetary rotation rate (Ω) and wind stress (τ) when dominated by wind forcing.

Table 1
Baseline Values of Planetary and Oceanic Parameters

Parameter	Value	Units
Planet radius (a)	10^{7}	m
Planet gravity (g)	20	m s^{-2}
Planet rotation rate (Ω)	0	s^{-1}
Substellar temperature ($T_{\rm sub}$)	3000	K
Liquidus ($T_{\rm liq}$)	2000	K
Temperature contrast within the ocean ($\Delta T = T_{\rm sub} - T_{\rm liq}$)	1000	K
Angular radius of the ocean ($\theta_p \approx \cos^{-1}\left(\frac{T_{\rm liq}}{T_{\rm sub}}\right)$)	2	
Horizontal scale of the ocean ($L \approx a\theta_p$)	2×10^{7}	m
Thermal expansion coefficient (α)	2×10^{-4}	K^{-1}
Heat capacity at constant pressure (c_p)	1800	J kg^{-1} K^{-1}
Buoyancy contrast within the ocean ($\Delta b = g\alpha\Delta T$)	4	m s^{-2}
Vertical viscosity (A_z)	10^{1}	m^{2} s^{-1}
Vertical diffusivity (k_z)	10^{-4}	m^{2} s^{-1}
Wind stress (τ)	0	N m^{-2}

It should be noted that the value of the vertical viscosity in this regime should be smaller than certain values to satisfy the momentum balance here. As we introduce in the beginning of this section, the momentum equation is in balance between the pressure gradient force and advection below the boundary layer. Thus, the vertical viscosity term is not allowed to be larger than advection. The specific values of vertical viscosity in Regime II will be discussed in Section 3 in detail.

As wind stress increases, the magma ocean depth reaches deeper and the horizontal velocity becomes larger, leading to intensified heat transport convergence (Figures 5(b), (d), and (f)). The increase in wind stress directly makes the horizontal divergence/convergence of mass transport larger, thus intensifying the vertical velocity. Thus, the magma ocean deepens with stronger vertical advection. A deeper magma ocean increases the vertical integral of density contrast, i.e., the pressure gradient force. Thus, the interior horizontal velocity becomes larger under stronger wind stress.

2.3. Regime III: Rotation-dominant Regime

In Sections 2.1 and 2.2, we present scaling laws assuming that the rotation effect is negligible. Here, we present scaling laws for the horizontal current speed, magma ocean depth, and ocean heat transport convergence when rotation plays a dominant role. In this regime, the Coriolis force balances the pressure gradient force (green brackets in Figure 1(a)). This so-called geostrophic balance regime has been extensively studied due to its application to Earth's oceans. Scaling laws derived for Earth's oceans can also be applied to thermally forced lava oceans as done in E. S. Kite et al. (2016). Here, we will briefly review the derivation. Interested readers can refer to textbooks such as G. K. Vallis (2017, 2019) for more information.

The derivation utilizes three relationships. First, by taking the vertical curl of the horizontal momentum equation and using the mass continuity, we can derive the linear vorticity equation

$$\beta v = f\frac{\partial w}{\partial z}, \tag{24}$$

where $\beta = 2\Omega\cos\phi/a$ denotes the gradient of the Coriolis coefficient $f = 2\Omega\sin\phi$ along the meridional direction, Ω denotes the planetary rotation rate, ϕ denotes latitude, and a denotes planet radius. In the linear vorticity equation, the left-hand side represents the advection of planetary vorticity, and the right-hand side represents the generation of vorticity by vortex stretching.

Second, by taking the vertical derivative of the momentum equation (geostrophic balance relation) and using the hydrostatic balance, we derive the thermal wind balance,

$$f\frac{\partial \boldsymbol{u}}{\partial z} = \boldsymbol{k} \times \nabla b, \tag{25}$$

where $\boldsymbol{u}$ denotes horizontal velocity and $\boldsymbol{k}$ denotes the unit vector pointing upward. The last set of relationships has to do with the driving force of the circulation. When wind forcing is weak, the dominant driver of the circulation is diffusion. Similar to previous cases, the heat/buoyancy will be in advection–diffusion balance (Equation (3)).

We can then write down the corresponding scales for Equations (24), (25), and (3) as

$$\beta U \sim f\frac{W}{D}, \tag{26a}$$

$$f\frac{U}{D} \sim \frac{\Delta b}{L}, \tag{26b}$$

$$D \sim \frac{k_z}{W}. \tag{26c}$$

It should be noted that we assume $U \sim V$ in the scaling analysis presented here. This assumption is valid for tidally locked lava planets, where the latitudinal and longitudinal extensions of the magma ocean are comparable. In other words, although U is not directly affected by the beta effect, it also obeys the Svedrup balance in accordance with V. From Equation (26), the characteristic scales for the magma ocean depth (D_{3t}) and horizontal velocity (U_{3t}) can be solved,

$$D_{3t} \sim \left(\frac{k_z f^2 L}{\beta \Delta b}\right)^{1/3},\ U_{3t} \sim \left(\frac{k_z \Delta b^2}{\beta f L^2}\right)^{1/3}. \tag{27}$$

Combining Equations (8) and (27), the scale for ocean heat transport convergence (H_{3t}) is expressed as

$$H_{3t} \sim \frac{\rho c_p}{g\alpha}\left(\frac{f k_z^2 \Delta b^4}{\beta^2 L^4}\right)^{1/3}. \tag{28}$$

Table 2
Summary of Scaling Laws under Varying Dominant Forcings and Regimes

Forcing	Regime	Ocean Depth (D)	Current Speed (U)	Heat Transport Convergence (H)
Thermal	I	$\left(\frac{k_z A_z L^2}{\Delta b}\right)^{1/5}$	$\left(\frac{\Delta b^2 k_z^3 L}{A_z^2}\right)^{1/5}$	$\frac{\rho c_p}{g\alpha}\left(\frac{k_z^4 \Delta b^6}{A_z L^2}\right)^{1/5}$
	II	$\left(\frac{k_z^2 L^2}{\Delta b}\right)^{1/5}$	$(\Delta b^2 k_z L)^{1/5}$	$\frac{\rho c_p}{g\alpha}\left(\frac{k_z^3 \Delta b^6}{L^2}\right)^{1/5}$
	III	$\left(\frac{k_z f^2 L}{\beta \Delta b}\right)^{1/3}$	$\left(\frac{k_z \Delta b^2}{\beta f L^2}\right)^{1/3}$	$\frac{\rho c_p}{g\alpha}\left(\frac{f k_z^2 \Delta b^4}{\beta^2 L^4}\right)^{1/3}$
Wind	I	$\left(\frac{\tau L}{\rho \Delta b}\right)^{1/2}$	$\left(\frac{\tau^3 L}{\rho^3 A_z^2 \Delta b}\right)^{1/2}$	$\frac{c_p}{g\alpha}\left(\frac{\tau^2}{\rho A_z}\right)$
	II	$\left(\frac{\tau^2 A_z^2 L^4}{\rho^2 \Delta b^3}\right)^{1/9}$	$\left(\frac{\tau A_z \Delta b^3 L^2}{\rho}\right)^{1/9}$	$\frac{c_p}{g\alpha}\left(\frac{\tau A_z}{L}\rho^2 \Delta b^3\right)^{1/3}$
	III	$\left(\frac{\tau f}{\rho \beta \Delta b}\right)^{1/2}$	$\left(\frac{\tau \Delta b}{\rho f \beta L^2}\right)^{1/2}$	$\frac{c_p}{g\alpha}\left(\frac{\tau \Delta b}{\beta L^2}\right)$

Note. In the scaling laws, k_z is the vertical diffusivity, A_z is the vertical viscosity, L is the horizontal scale of the magma ocean, Δb is the horizontal buoyancy contrast, τ is the wind stress, f is the Coriolis parameter, β is the meridional gradient of the Coriolis parameter, ρ is the ocean density, g is gravity, α is the thermal expansion coefficient, and c_p is the heat capacity at constant pressure.

When wind forcing is the main driving force of the circulation, we need to consider the interior vertical motions induced by the curl of wind stress, a phenomenon known as Ekman pumping. The vertical velocity at the base of the Ekman layer W_E follows (J. Pedlosky 1996; R. H. Stewart 2008; G. K. Vallis 2019)

$$W_E = -\frac{1}{\rho}\,\mathrm{curl}_z\left(\frac{\tau}{f}\right) \sim \frac{\tau}{\rho L f}, \tag{29}$$

where τ is the wind stress and curl_z represents the vertical component of the curl. Replacing Equation (26c) with Equation (29), we instead get the following scaling laws for the magma ocean depth (D_{3w}) and horizontal velocity (U_{3w}):

$$D_{3w} \sim \left(\frac{\tau f}{\rho \beta \Delta b}\right)^{1/2},\ U_{3w} \sim \left(\frac{\tau \Delta b}{\rho f \beta L^2}\right)^{1/2}. \tag{30}$$

Substituting Equation (30) into Equation (8), we obtain the characteristic scale for ocean heat transport convergence (H_{3w}),

$$H_{3w} \sim \frac{c_p}{g\alpha}\frac{\tau \Delta b}{\beta L^2}. \tag{31}$$

The scaling laws for the magma ocean depth (D), horizontal current speed (U), and ocean heat transport convergence (H) under varying dominant forcings and regimes are summarized in Table 2.

When wind forcing is absent or weak, Equations (27) and (28) suggest that the magma ocean depth, horizontal velocity, and ocean heat transport convergence are controlled by the vertical diffusivity, planetary rotation rate, and surface temperature difference. The effects of vertical diffusivity have been illustrated many times previously. In Figures 6(a), (c), and (e), the results under varying rotation rates and substellar temperatures are presented. As the rotation rate increases, the horizontal velocity reduces under the geostrophic balance constraint. Thus, the vertical velocity decreases from mass continuity, leading to a deeper magma ocean. As the substellar temperature increases, the pressure gradient force is larger, resulting in stronger horizontal and vertical velocities. Meanwhile, the magma ocean depth, determined by the advection–

diffusion balance, is decreased. Dominated by the variation of current speed, ocean heat transport convergence decreases with increasing rotation rate, while it increases as the substellar temperature becomes higher (Equation (28)).

In the presence of strong wind forcing, the wind stress, planetary rotation rate, and substellar temperature could exert influences on the magma ocean depth, horizontal velocity, and heat transport convergence (Equations (30) and (31)). Here we present results under varying wind stresses and planetary rotation rates (Figures 6(b), (d), and (f)). As the rotation rate increases, the magma ocean depth remains unchanged, accompanied by a smaller horizontal velocity. According to the geostrophic balance and Ekman pumping relationship, both horizontal and vertical velocities will decrease with rotation rate at the same rate (Equations (26b) and (29)). Thus, the effect of varying rotation rates on magma ocean depth could vanish (Equation (26a)). Weaker ocean circulation results in decreased ocean heat transport convergence (Equation (31)).

The influences of varying amplitudes of wind stress are presented in Figures 6(b), (d), and (f). As wind stress increases, both ocean depth and horizontal velocity increase. This is because Ekman pumping (subduction) strengthens under larger wind stress, which deepens the magma ocean. With a deeper ocean, the vertical integral of buoyancy contrast increases, leading to a larger pressure gradient force and then stronger horizontal velocity. Proportional to current speed and ocean depth, ocean heat transport convergence increases as wind stress becomes stronger.

3. Parameter Regimes for the Scalings

We have presented different scaling laws in different dynamical regimes in Section 2, based on the balance between the horizontal pressure gradient force and varying terms. In this section, we attempt to discuss the parameter space where each of the scaling laws is applicable. Especially, the parameter regime is discussed in two parts: thermal-forcing-dominated and wind-forcing-dominated systems.

3.1. Thermal-forcing-dominated System

In Regime I, the pressure gradient force is balanced by vertical viscosity; i.e., the vertical viscosity term is greater than both the advection and Coriolis force. Thus, the relationship between the vertical viscosity, advection, and Coriolis force can be expressed as

$$A_z \frac{U}{D^2} > \max\left\{\frac{U^2}{L}, fU\right\}. \tag{32}$$

Substituting U_{1t} and D_{1t} from Equation (7) into Equation (32), we derive the relationship between varying parameters,

$$A_z > \max\left\{k_z, \Omega^{\frac{5}{3}}\left(\frac{k_z L^2}{\Delta b}\right)^{\frac{2}{3}}\right\}. \tag{33}$$

Thus, the magma ocean will be in Regime I when the vertical viscosity coefficient is larger than certain values.

Regime II occurs when the nonlinear advection term is larger than both the vertical viscosity and Coriolis force, i.e.,

$$\frac{U^2}{L} > \max\left\{A_z \frac{U}{D^2}, fU\right\}. \tag{34}$$

Substituting the scaling laws for the horizontal current speed and ocean depth in Regime II, i.e., U_{2t} and D_{2t} from Equation (16), into Equation (34), we obtain

$$A_z < k_z, \Omega < \left(\frac{\Delta b^2 k_z}{L^4}\right)^{\frac{1}{5}}. \tag{35}$$

Thus, the magma ocean will be in Regime II when both the vertical viscosity coefficient and planetary rotation rate are smaller than certain values.

The magma ocean is in Regime III when the Coriolis force is greater than both the vertical viscosity and nonlinear advection, which is expressed as

$$fU > \max\left\{A_z \frac{U}{D^2}, \frac{U^2}{L}\right\}. \tag{36}$$

It is worth noting that Equation (36) can also be represented as both the vertical Ekman number ($\mathrm{E}_z = \frac{A_z}{fD^2}$) and the Rossby number ($\mathrm{Ro} = \frac{U}{fL}$) being smaller than 1 (R. H. Stewart 2008; G. K. Vallis 2019). Employing the scaling laws for the horizontal current speed and ocean depth in Regime III, i.e., U_{3t} and D_{3t} from Equation (27), Equation (36) becomes

$$\Omega > \max\left\{A_z^{\frac{3}{5}}\left(\frac{\Delta b}{k_z La}\right)^{\frac{2}{5}}, \left(\frac{k_z \Delta b^2 a}{L^5}\right)^{\frac{1}{5}}\right\}. \tag{37}$$

Equations (33), (35), and (37) present the criteria for the three scaling laws to hold when wind forcing is negligible compared to thermal forcing. To give an example, we assume a super-Earth type of configuration: $k_z \sim 10^{-4}$ m^2 s^{-1}, $g \sim 20$ m s^{-2}, $\alpha \sim 2 \times 10^{-4}$ K^{-1}, $\Delta T \sim 10^3$ K, $\Delta b \sim 4$ m s^{-2}, $L \sim 2 \times 10^7$ m, and $a \sim 10^7$ m. The criteria for the three regimes follow

$$\begin{aligned} \text{Regime I:}\ & A_z > ax\{10^{-4}, 5 \cdot 10^6 \times \Omega^{\frac{5}{3}}\}, \\ \text{Regime II:}\ & A_z < 10^{-4}, \Omega < 4 \times 10^{-7}, \\ \text{Regime III:}\ & \Omega > \max\{10^{-4} \times A_z^{\frac{3}{5}}, 4 \times 10^{-7}\}. \end{aligned} \tag{38}$$

In Figure 7(a), we mark the three regimes using different colors in the (Ω, A_z) parameter space. Since the viscosity of the molten rock (i.e., the magma ocean) is usually around 10^{-5} or 10^{-4} m^2 s^{-1} (Y. Zhang et al. 2022), and the orbital period of a typical tidally locked lava planet (such as Kepler-10b, CoRot-7b, 55 Cnc e, and K2-141b) is around 1 Earth day (N. M. Batalha et al. 2011; A. Léger et al. 2011; V. Bourrier et al. 2018; L. Malavolta et al. 2018; C. L. Brinkman et al. 2023), the rotation-dominant Regime III is likely to be the most relevant.

With a 10^{-4} m^2 s^{-1} viscosity, Regimes I and II will only be relevant if the orbital period is longer than ∼180 Earth days. This may be achieved on slowly rotating exoplanets or moons, whose magma ocean is created by giant impacts (L. T. Elkins--Tanton 2012). It should be noted that although the molecular viscosity/diffusivity is generally weak, when turbulence is present, the eddy viscosity/diffusivity might be much greater than 10^{-4} m^2 s^{-1}. For example, in Earth's oceans, the vertical eddy viscosity/diffusivity could reach 10^{-3}–10^{-1} m^2 s^{-1} in places with strong topography, winds, and baroclinic eddies (C. Luo et al. 2023; A. Sentchev et al. 2023). Besides these energy sources, lava worlds are also subject to strong tidal forcing, and that can further trigger internal gravity waves and

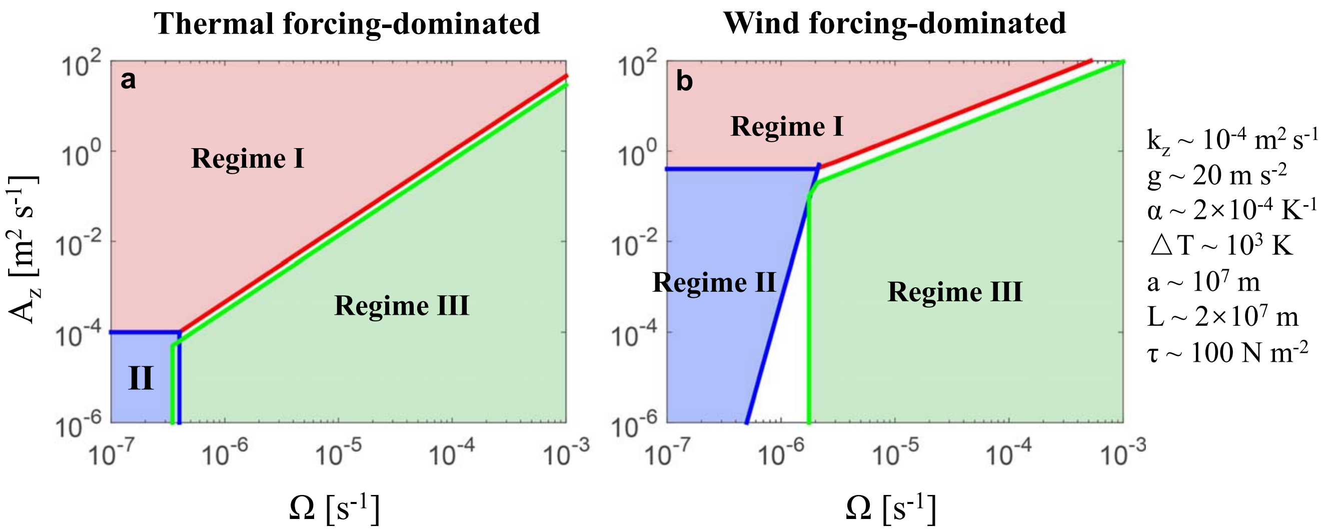

Figure 7. Regime diagram in (Ω, A_z)-space in thermal-forcing-dominated (a) and wind-forcing-dominated (b) systems. The regions in red, blue, and green colors correspond to the parameter space in Regimes I (viscosity-dominant), II (advection-dominant), and III (rotation-dominant), respectively. The parameters used to obtain this diagram, including vertical diffusivity (k_z), gravity (g), thermal expansion coefficient (α), temperature difference (ΔT), planet radius (a), horizontal range of the magma ocean (L), and wind stress (τ), are listed on the right side of panel (b). Note that wind stress is not included ($\tau = 0$) in the thermal-forcing-dominated case. Due to the simplicity of these scaling laws, there is some overlap between different regimes, and blank areas are not resolved by these scalings.

turbulent mixing in the ocean (T. H. Bell 1975; S. G. L. Smith & W. Young 2001). With a larger eddy viscosity of 10^{-2} m^2 s^{-1}, the magma ocean could switch to Regime I with an orbital period beyond ∼10 Earth days.

3.2. Wind-forcing-dominated System

Following the same approach, in Regime I, the vertical viscosity term should be greater than both the nonlinear advection and Coriolis force, i.e., Equation (32). Employing the scaling laws for the horizontal current speed (U_{1w}) and ocean depth (D_{1w}) in Regime I from Equation (12), we get the following criterion:

$$A_z > \max\left\{\left(\frac{\tau_x^5 L}{\rho^5 \Delta b^3}\right)^{\frac{1}{4}}, \Omega\frac{\tau_x L}{\rho \Delta b}\right\}. \tag{39}$$

In Regime II, the nonlinear advection should be larger than both the vertical viscosity and Coriolis force. Substituting the scaling laws for U_{2w} and D_{2w} from Equation (22) into Equation (34), we obtain

$$A_z < \left(\frac{\tau_x^5 L}{\rho^5 \Delta b^3}\right)^{\frac{1}{4}}, \Omega < A_z^{\frac{1}{9}}\left(\frac{\Delta b^3 \tau_x}{\rho L^7}\right)^{1/9}. \tag{40}$$

In Regime III, the Coriolis force dominates over both the vertical viscosity and nonlinear advection, i.e., Equation (36). Adopting the scaling laws for D_{3w} and U_{3w} from Equation (30), we obtain

$$\Omega > \max\left\{A_z\frac{\rho \Delta b}{\tau a}, \left(\frac{\tau \Delta b}{\rho L^4}\right)^{\frac{1}{4}}\right\}. \tag{41}$$

We revisit the example mentioned in Section 3.1 assuming $\tau \sim 100$ N m^{-2} (W. Kang et al. 2021), and Equations (39)–(41) can be written as

$$\begin{aligned} \text{Regime I:}\ & A_z > \max\{0.4,\ 2 \cdot 10^5 \times \Omega\},\\ \text{Regime II:}\ & A_z < 0.4,\ \Omega < 2 \cdot 10^{-6} \times A_z^{1/9},\\ \text{Regime III:}\ & \Omega > \max\{10^{-5} \times A_z,\ 2 \times 10^{-6}\}. \end{aligned} \tag{42}$$

The regime diagram for a wind-dominated system is presented in Figure 7(b). Given the typical vertical viscosity of the magma ocean ($A_z \sim 10^{-4}$ m^2 s^{-1}) and the rotation rate of tidally locked lava planets ($\Omega \sim 10^{-4}$ m^{-1}), the ocean circulation will be most likely in the rotation-dominant Regime III. The dominant role of rotation in the ocean circulation works in both thermal-forcing-dominated and wind-forcing-dominated systems. With a 10^{-4} m^2 s^{-1} viscosity, the magma ocean could shift to Regime II when the orbital period is beyond ∼100 Earth days. This criterion may be achieved on those slowly rotating planets where magma oceans occur due to giant impacts (L. T. Elkins-Tanton 2012).

When dominated by strong wind forcing, Regime I will only be relevant when the vertical viscosity is larger than 0.4 m^2 s^{-1}. Meanwhile, the rotation period should be beyond ∼30 Earth days with a viscosity of 0.4 m^2 s^{-1}. This requirement for viscosity is relatively strict and may be satisfied by the presence of very strong eddy viscosity (C. Luo et al. 2023; A. Sentchev et al. 2023).

4. Conclusions

On tidally locked lava planets, a magma ocean may form on the permanent dayside. Circulation of the magma ocean can be driven by the heterogeneity of stellar radiation and the stress created by the atmosphere flow from the hot dayside to the cold nightside (T. Castan & K. Menou 2011; T. G. Nguyen et al. 2020; W. Kang et al. 2021) as sketched in Figure 2. The strength and depth of the ocean circulation follow different scaling laws depending on whether wind forcing or thermal forcing is dominant and the dominant balance of the momentum equation (Figure 1). In this study, we explore the controlling factors of the strength of ocean circulation, the depth of the magma ocean, and the ocean heat transport convergence driven by stellar and wind forcings in three dynamic regimes: nonrotating viscosity-dominant Regime I, nonrotating inviscid limit Regime II, and rotation-dominant Regime III. From Regimes I to III, the pressure gradient force is predominantly balanced by vertical viscosity, nonlinear advection, and the Coriolis force, respectively.

When the main driving force of the ocean circulation is thermal forcing, the magma ocean depth, horizontal velocity, and ocean heat transport convergence scale with vertical diffusivity, vertical viscosity, planetary rotation rate, and surface temperature/buoyancy difference. Utilizing the dominant momentum balance, mass continuity, and advection–diffusion balance, we obtain scaling laws for each of the three dynamic regimes, which are summarized in Table 2. When the main driving force is wind stress, the interior velocity is no longer internally determined but is induced by the horizontal convergence/divergence of mass transport in the wind-driven boundary layer. Utilizing the dominant momentum balance, mass continuity, and boundary layer transport, we obtain scaling laws for ocean depth, current speed, and ocean heat transport convergence for the three dynamic regimes. The results are summarized in Table 2. For each scaling law, we determine its applicable conditions in Section 3. For Regime I only, we conducted a set of 2D numerical simulations. The numerical results match the scaling prediction reasonably well. The numerical examination of Regime II and Regime III is left for future work.

Following these scaling laws, we examined the sensitivity of magma ocean depth, current speed, and ocean heat transport convergence to various controlling parameters, including the planetary rotation rate, substellar temperature, wind stress amplitude, and diffusivity/viscosity. Substituting parameters for a typical lava super-Earth, we found the rotation-dominant Regime III to be the most relevant. Scaling laws predict a magma ocean depth that ranges from a few meters to a few hundred meters and an ocean heat transport convergence that is smaller than the stellar insolation by 1–4 orders of magnitude, in line with previous work by E. S. Kite et al. (2016) and Part I.

It should be noted that, although we treat wind stress, thermal forcing, rotation rate, and diffusivity/viscosity as independent parameters in this work, they are intrinsically related. For example, wind stress τ is proportional to the square of the atmospheric flow speed, which in turn scales with the substellar temperature $\sqrt{T_{\mathrm{sub}}}$ (W. Kang et al. 2021). This means that τ should scale with T_{sub}. In turn, hotter planets usually surround their host star at a closer distance, which yields a faster rotation rate, assuming star luminosity is fixed. As the distance between the star and planet decreases, the tidal forcing is also likely to increase, which may induce stronger eddy diffusivity and viscosity (T. H. Bell 1975; S. G. L. Smith & W. Young 2001).

Acknowledgments

We express our gratitude to Feng Ding for his insightful discussions. J.Y. is supported by NSFC under grant Nos. 42075046, 42275134, and 42161144011. This work has been supported by the science research grants from the China Manned Space Project (No. CMS-CSST-2021-B09). W.K. is supported by the MIT startup fund.

The 2D model employed in this study was developed by the authors and is available at https://github.com/YanhongLai/Two-dimensional-model-for-magma-ocean-on-lava-worlds.git. The simulation data used are archived in Zenodo at doi:10.5281/zenodo.11467142.

ORCID iDs

Yanhong Lai https://orcid.org/0000-0001-9700-9121
Wanying Kang https://orcid.org/0000-0002-4615-3702
Jun Yang https://orcid.org/0000-0001-6031-2485

References

Batalha, N. M., Borucki, W. J., Bryson, S. T., et al. 2011, ApJ, 729, 27
Bell, T. H. 1975, JFM, 67, 705
Boukare, C.-É., Cowan, N. B., & Badro, J. 2022, ApJ, 936, 148
Bourrier, V., Dumusque, X., Dorn, C., et al. 2018, A&A, 619, A1
Brinkman, C. L., Weiss, L. M., Dai, F., et al. 2023, AJ, 165, 88
Castan, T., & Menou, K. 2011, ApJL, 743, L36
Chao, K.-H., deGraffenried, R., Lach, M., et al. 2021, ChEG, 81, 125735
Demory, B.-O., Gillon, M., Deming, D., et al. 2011, A&A, 533, A114
Dingwell, D. B., Courtial, P., Giordano, D., & Nichols, A. R. L. 2004, E&PSL, 226, 127
Dumusque, X., Bonomo, A. S., Haywood, R. D., et al. 2014, ApJ, 789, 154
Elkins-Tanton, L. T. 2012, AREPS, 40, 113
Ferrari, R., & Ferreira, D. 2011, OcMod, 38, 171
Ghosh, D. B., & Karki, B. B. 2011, GeCoA, 75, 4591
Hammond, M., & Pierrehumbert, R. T. 2018, ApJ, 869, 65
Haynes, W. M. 2014, CRC Handbook of Chemistry and Physics (Boca Raton, FL: CRC press)
Ingersoll, A. P., Summers, M. E., & Schlipf, S. G. 1985, Icar, 64, 375
Jiang, W., Wu, L., & Liu, Q. 2021, FrEaS, 9, 396
Kang, W., Ding, F., Wordsworth, R., & Seager, S. 2021, ApJ, 906, 67
Kite, E. S., Fegley, B., Jr, Schaefer, L., & Gaidos, E. 2016, ApJ, 828, 80
Léger, A., Grasset, O., Fegley, B., et al. 2011, Icar, 213, 1
Léger, A., Rouan, D., Schneider, J., et al. 2009, A&A, 506, 287
Luo, C., Gao, G., Xu, M., Yin, B., & Lv, X. 2023, Journal of Marine Science and Engineering, 11, 1487
Malavolta, L., Mayo, A. W., Louden, T., et al. 2018, AJ, 155, 107
Meier, T. G., Bower, D. J., Lichtenberg, T., Hammond, M., & Tackley, P. J. 2023, A&A, 678, A29
Monteux, J., Andrault, D., & Samuel, H. 2016, E&PSL, 448, 140
Munk, W., & Wunsch, C. 1998, DSRI, 45, 1977
Nguyen, T. G., Cowan, N. B., Banerjee, A., & Moores, J. E. 2020, MNRAS, 499, 4605
Pedlosky, J. 1996, Ocean Circulation Theory (Berlin: Springer)
Schaefer, L., & Fegley, B. 2009, ApJ, 703, L113
Sentchev, A., Yaremchuk, M., Bourras, D., Pairaud, I., & Fraunié, P. 2023, JAtOT, 40, 1291
Smith, S. G. L., & Young, W. 2001, JPO, 32, 1554
Solomatov, V. 2007, Magma Oceans and Primordial Mantle Differentiation, in Evolution of the Earth. Treatise on Geophysics, Vol. 9, ed. G. Schubert (Amsterdam: Elsevier), 91
Sterl, A. 2017, Roy. Netherland Met. Office. Tech. Rep., 361, 23
Stewart, R. H. 2008, Introduction To Physical Oceanography (Gainesville, FL: Univ. Press of Florida)
Sun, Y., Zhou, H., Liu, X., Yin, K., & Lu, X. 2020, E&PSL, 551, 116556
Valencia, D., Ikoma, M., Guillot, T., & Nettelmann, N. 2010, A&A, 516, A20
Vallis, G. K. 2017, Atmospheric and Oceanic Fluid Dynamics (Cambridge: Cambridge Univ. Press)
Vallis, G. K. 2019, Essentials of Atmospheric and Oceanic Dynamics (Cambridge: Cambridge Univ. Press)
Von Braun, K., Tabetha, S. B., Ten Brummelaar, T. A., et al. 2011, ApJ, 740, 49
Wang, S., & Yang, J. 2021, ApJ, 907, 28
Waterhouse, A. F., MacKinnon, J. A., Nash, J. D., et al. 2014, JPO, 44, 1854
Wunsch, C., & Ferrari, R. 2004, AnRFM, 36, 281
Yang, J., Zhang, Y., Fu, Z., et al. 2023, NatAst, 7, 1070
Zhang, Y., Zhang, N., & Tian, M. 2022, AcGch, 41, 568